A&A 627, A88 (2019)
https://doi.org/10.1051/0004-6361/201935265

Astronomy & Astrophysics

Black hole mass estimates in quasars

A comparative analysis of high- and low-ionization lines

P. Marziani[1], A. del Olmo[2], M. A. Martínez-Carballo[3], M. L. Martínez-Aldama[4], G. M. Stirpe[5], C. A. Negrete[6,⋆], D. Dultzin[6], M. D'Onofrio[7,⋆⋆], E. Bon[8], and N. Bon[8]

[1] INAF, Osservatorio Astronomico di Padova, vicolo dell' Osservatorio 5, 35122 Padova, Italy
e-mail: paola.marziani@oapd.inaf.it
[2] Instituto de Astrofisíca de Andalucía, IAA-CSIC, Glorieta de la Astronomia s/n, 18008 Granada, Spain
e-mail: chony@iaa.es
[3] Departamento de Matemática Aplicada and IUMA, Universidad de Zaragoza, 50009 Zaragoza, Spain
e-mail: gelimc@unizar.es
[4] Center for Theoretical Physics, Polish Academy of Science, 02-668 Warsaw, Poland
[5] INAF, Osservatorio di Astrofisica e Scienza dello Spazio, 40129 Bologna, Italy
[6] Instituto de Astronomía, UNAM, Mexico D.F. 04510, Mexico
[7] Dipartimento di Fisica & Astronomia "Galileo Galilei", Università di Padova, Vicolo ell'Osservatorio 3, 35122 Padova, Italy
[8] Astronomical Observatory, Belgrade, Serbia

Received 11 February 2019 / Accepted 1 May 2019

ABSTRACT

Context. The inter-line comparison between high- and low-ionization emission lines has yielded a wealth of information on the structure and dynamics of the quasar broad line region (BLR), including perhaps the earliest unambiguous evidence in favor of a disk + wind structure in radio-quiet quasars.
Aims. We carried out an analysis of the CIVλ1549 and Hβ line profiles of 28 Hamburg-ESO high-luminosity quasars and of 48 low-z, low-luminosity sources in order to test whether the width of the high-ionization line CIVλ1549 could be correlated with Hβ and be used as a virial broadening estimator.
Methods. We analyze intermediate- to high-S/N, moderate-resolution optical and near-infrared (NIR) spectra covering the redshifted CIVλ1549 and Hβ over a broad range of luminosity $\log L \sim 44-48.5$ [erg s^{-1}] and redshift (0−3), following an approach based on the quasar main sequence.
Results. The present analysis indicates that the line width of CIVλ1549 is not immediately offering a virial broadening estimator equivalent to Hβ. At the same time a virialized part of the BLR appears to be preserved even at the highest luminosities. We suggest a correction to FWHM(CIVλ1549) for Eddington ratio (using the CIVλ1549 blueshift as a proxy) and luminosity effects that can be applied over more than four dex in luminosity.
Conclusions. Great care should be used in estimating high-L black hole masses $M_{\rm BH}$ from CIVλ1549 line width. However, once a corrected FWHM CIVλ1549 is used, a CIVλ1549-based scaling law can yield unbiased $M_{\rm BH}$ values with respect to the ones based on Hβ with sample standard deviation ≈0.3 dex.

Key words. quasars: general – quasars: emission lines – quasars: supermassive black holes – line: profiles – ISM: jets and outflows

1. Introduction

Type-1 active galactic nuclei (AGNs) and quasars show the same broad optical-UV lines almost always accompanied by broad permitted FeII emission (e.g., Vanden Berk et al. 2001). However, even among type-1 sources we face a large diversity in observational manifestations involving line profiles, internal line shifts as well as emission line intensity ratios (e.g., Sulentic et al. 2000a; Bachev et al. 2004; Yip et al. 2004; Kuraszkiewicz et al. 2009; Zamfir et al. 2010; Shen & Ho 2014, and Sulentic & Marziani 2015 for a recent review). Broad line measurements involving Hβ line width and FeII strength are not randomly distributed but instead define a quasar "main sequence" (MS; e.g., Boroson & Green 1992; Sulentic et al. 2000a; Shen & Ho 2014). The MS can be traced in an optical plane defined by FeII emission prominence and the hydrogen Hβ line width. The FeII strength is parametrized by the intensity ratio involving the FeII blue blend at 4570 Å and broad Hβ, that is, $R_{\rm FeII}$ = I(FeIIλ4570)/I(Hβ), and the hydrogen Hβ line width by its full width at half maximum. Along the MS, sources with higher $R_{\rm FeII}$ show narrower broad Hβ (Population A, $FWHM(\mathrm{H}\beta) \lesssim 4000\,\mathrm{km\,s^{-1}}$, Sulentic et al. 2000a). Lower $R_{\rm FeII}$ is associated with sources with broader Hβ profiles (Pop. B with $FWHM(\mathrm{H}\beta) \gtrsim 4000\,\mathrm{km\,s^{-1}}$, Sulentic et al. 2011). A glossary of the MS-related terminology is provided in Appendix A.

Studies of the Balmer lines have played a prominent role in characterizing the MS and the properties of the broad-line-emitting region (BLR) in low-z ($\lesssim$0.8) quasars with Hβ providing information for the largest number of sources (e.g., Osterbrock & Shuder 1982; Wills et al. 1985; Sulentic 1989; Zamfir et al. 2010; Hu et al. 2012; Steinhardt & Silverman 2013; Shen 2016, for a variety of observational and statistical approaches). The most important application of the FWHM Hβ has been its use as a virial broadening estimator (VBE) to derive black hole masses ($M_{\rm BH}$)

⋆ CONACyT research fellow, Instituto de Astronomía, UNAM.
⋆⋆ INAF associate, Osservatorio Astronomico di Padova.

from single-epoch observations of large samples of quasars (e.g., McLure & Jarvis 2002; McLure & Dunlop 2004; Vestergaard & Peterson 2006; Assef et al. 2011; Shen 2013; Peterson 2014, and references therein). The underlying assumption is that the Hβ line width provides the most reliable VBE, which is likely to be the case, albeit with some caveats (e.g., Trakhtenbrot & Netzer 2012, see also Shen 2013, Peterson 2014 for reviews).

Balmer lines provide a reliable VBE up to $z \lesssim 2$ (Matsuoka et al. 2013; Karouzos et al. 2015) at cosmic epochs of less than a few gigayears. The importance of having a reliable VBE at even earlier cosmic epochs cannot be underemphasized. The entire scenario of early structure formation is affected by inferences from estimates of quasar black hole masses. Overestimates of $M_{\rm BH}$ by lines whose broadening is in excess of the virial one can have implications for the quasar mass function. Also, at high redshift ($z \gtrsim 6$) when the Universe was less than 1 billion years old, overestimates have further implications for the formation and mass spectrum of the seed black holes (Latif & Ferrara 2016) that may have been responsible, along with Pop. III stars, for the reionization of the process at $z \sim 7{-}10$ (e.g., Gallerani et al. 2017, for a review).

Strong and relatively unblended CIVλ1549 has been the best candidate for a VBE beyond $z \sim 1.5$, where Hβ is shifted into the IR domain. CIVλ1549 can be observed up to redshift $z \approx 6$ with optical spectrometers, and in the near-infrared (NIR) bands up to redshift $z \approx 7.5$ (Bañados et al. 2018) and beyond. Can CIVλ1549 be used as an immediate surrogate for Hβ when Hβ is invisible or hard to obtain? Before attempting an answer to this question, two considerations are in order.

First, measurements of the CIVλ1549 line profiles remain of uncertain interpretation without a precise determination of the quasar rest frame: an accurate z measurement is not easy to obtain from broad lines, and redshift determinations at $z \gtrsim 1$ from optical survey data suffer systematic biases as large as several hundreds of kilometres per second (Hewett & Wild 2010; Shen et al. 2016). Reliable studies tie CIV measurements to a rest frame derived from the Hβ narrow component (+[OIII]$\lambda\lambda$4959,5007 whenever applicable; e.g., Mejía-Restrepo et al. 2016; for problems in the use of [OIII]$\lambda\lambda$4959,5007, see Zamanov et al. 2002; Hu et al. 2008).

Second, significant CIVλ1549 blueshifts are observed over a broad range in redshift and luminosity, from the nearest Seyfert 1 galaxies to the most powerful radio-quiet quasars (Wills et al. 1993; Sulentic et al. 2007, 2017; Richards et al. 2011; Coatman et al. 2016; Shen 2016; Bischetti et al. 2017; Bisogni et al. 2017; Vietri 2017). Measurements of the CIVλ1549 profile velocity displacement provide an additional dimension to a 4D "eigenvector 1" (4DE1) space built on parameters that are observationally independent ("orthogonal") and related to different physical aspects (Sulentic & Marziani 2015). Inclusion of the CIVλ1549 shift as a 4DE1 parameter was motivated by the earlier discovery of internal redshift differences between low- and high-ionization lines (Burbidge & Burbidge 1967; Gaskell 1982; Tytler & Fan 1992; Brotherton et al. 1994a; Corbin & Boroson 1996; Marziani et al. 1996).

The current interpretation of the BLR in quasars sees the broad lines arising in a region that is physically and dynamically composite (e.g., Collin-Souffrin et al. 1988; Elvis 2000; Ferland et al. 2009; Kollatschny & Zetzl 2013; Grier et al. 2013; Du et al. 2016). CIVλ1549 is a doublet originating from an ionic species of ionization potential (IP) four times larger than Hydrogen (54 eV vs. 13.6 eV), and is therefore a prototypical high-ionization line (HIL). The line is mainly produced by collisional excitation from the ground state $^2S_0$ to $^2S_{\frac{1}{2},\frac{3}{2}}$ at the temperature of photo-ionized BLR gas ($T \sim 10^4$ K, Netzer 1990) in the fully ionized zone of the line-emitting gas. Empirically, the line is relatively strong (rest frame equivalent width $W \sim 10{-}100$ Å depending on the source location on the MS) and only moderately contaminated on the red side (red shelf) by HeIIλ1640 and OIII] λ1663 plus weak emission from FeII$_{\rm UV}$ multiplets (Fine et al. 2010). The Balmer line Hβ assumed to be representative of the low-ionization lines (LILs, from ionic species with IP $\lesssim 20$ eV) is instead enhanced in a partially ionized zone due to the strong X-ray emission of quasars and to the large column density of the line-emitting gas ($N_{\rm c} \gtrsim 10^{23}$ cm^{-2}; Kwan & Krolik 1981). Comparison of Hβ and CIVλ1549 profiles in the same sources tells us that they provide independent inputs to BLR models – their profiles can be dissimilar and several properties uncorrelated (see, e.g., Fig. C2 of Mejía-Restrepo et al. 2016).

It is possible to interpret Hβ and CIVλ1549 profiles as associated with two sub-regions within the BLR (e.g., Baldwin et al. 1996; Hall et al. 2003; Leighly 2004; Snedden & Gaskell 2004; Czerny & Hryniewicz 2011; Plotkin et al. 2015): one emitting predominantly LILs (e.g., Dultzin-Hacyan et al. 1999; Matsuoka et al. 2008), and a second emitting predominantly HILs, associated with gas outflows and winds (e.g., Richards et al. 2011; Yong et al. 2018). This view is in accordance with early models of the BLR structure involving a disk and outflow or wind component (Collin-Souffrin et al. 1988; Elvis 2000). Intercomparison of CIVλ1549 and Hβ at low z and moderate luminosity provided the most direct observational evidence that this is the case at least for radio-quiet (RQ) quasars (Corbin & Boroson 1996; Sulentic et al. 2007; Wang et al. 2011; Coatman et al. 2016). Modeling involves a disk + wind system (e.g., Proga et al. 2000; Proga & Kallman 2004; Flohic et al. 2012; Sdowski et al. 2014; Vollmer et al. 2018, for different perspectives), although the connection between disk structure and BLR (and hence the Hβ and CIVλ1549 emitting regions) is still unclear.

There are additional caveats, as the CIVλ1549 blueshifts are not universally detected. Their amplitude is a strong function of the location along the MS (Sulentic et al. 2000b, 2007; Sun et al. 2018). Large blueshifts are clearly detected in Population A, with sources accreting at relatively high rates, and reach extreme values for quasars at the high-$R_{\rm FeII}$ end along the MS. In Pop. B, the wind component is not dominating the line broadening of CIVλ1549 at moderate luminosity; conversely, the CIVλ1549 and Hβ line profile intercomparison indicates that the dynamical relevance of the CIVλ1549 blueshift is small, that is, the ratio between the centroid at half-maximum $c\left(\frac{1}{2}\right)$ and the FWHM is $\ll$1 (Sulentic et al. 2007). Reverberation mapping studies indicate that the velocity field is predominantly Keplerian (Pei et al. 2017 and references therein for the prototypical source NGC 5548, Denney et al. 2010; Grier et al. 2013), and that the CIVλ1549 emitting region is closer to a continuum source than that of Hβ (e.g., Peterson & Wandel 2000; Kaspi et al. 2007; Trevese et al. 2014). The issue is complicated by luminosity effects on the CIVλ1549 shifts that may have gone undetected at low redshifts. Both Pop. A and B sources at $\log L \gtrsim 47$ erg s^{-1} show large amplitude blueshifts in CIVλ1549 (Sulentic et al. 2017; Bisogni et al. 2017; Vietri et al. 2018). The present work considers the trends associated with the MS as well as the luminosity effects that may appear second-order in low-luminosity samples to provide corrections to the FWHM of Hβ and ultimately a scaling law based on CIVλ1549 FWHM and UV continuum luminosity that may be unbiased with respect to Hβ and with a reasonable scatter.

The occurrence of CIVλ1549 large shifts challenges the suitability of the CIVλ1549 profile broadening as a VBE for $M_{\rm BH}$ estimates (see e.g., Shen 2013, for a review). Results at low redshift suggest that the CIVλ1549 line is completely unsuitable for part of Pop. A sources (Sulentic et al. 2007). A similar conclusion was reached at $z \approx 2$ on a sample of 15 high-luminosity quasars (Netzer et al. 2007). More recent work tends to confirm that the CIVλ1549 line width is not straightforwardly related to virial broadening (e.g., Mejía-Restrepo et al. 2016). However, the CIVλ1549 line is strong and observable up to $z \approx 6$ with optical spectrometers. It is so highly desirable to have a consistent VBE up to the highest redshifts that various attempts (e.g., Brotherton et al. 2015) have been made to rescale CIVλ1549 line width estimators to the width of LILs such as Hβ and MgIIλ2800. Several conflicting claims have recently been made on the valid use of CIVλ1549 width in high-redshift quasars (e.g., Assef et al. 2011; Shen & Liu 2012; Denney et al. 2012; Karouzos et al. 2015; Coatman et al. 2017; Mejía-Restrepo et al. 2018a).

From the previous outline we infer that a proper approach to testing the suitability of the CIVλ1549 line width as a VBE is to compare CIVλ1549 and Hβ profiles along the quasar MS, and to extend the luminosity range including intermediate-to-high redshift ($\gtrsim$1.4) sources when Hβ is usually not covered by optical observations. A goal of this paper is to analyze the factors yielding large discrepancies between the $M_{\rm BH}$ estimates from Hβ and CIVλ1549, with a focus on the aspect and physical factors affecting the broadening of the two lines.

The quasar sample used in the present paper joins two samples with both Hβ and CIVλ1549 data, one at low luminosity and redshift ($\lesssim$0.7, Sulentic et al. 2007), and one at high luminosity, in the range $1.5 \lesssim z \lesssim 3$ presented and analyzed by Sulentic et al. (2017, hereafter Paper I). The sample provides a wide coverage in luminosity and Eddington ratio (Sect. 2); Hβ line coverage for each CIVλ1549 observation; and consistent analysis of the line profiles of both CIVλ1549 and Hβ (Sect. 3). Our approach is intended to overcome some of the sample-dependent difficulties encountered by past studies. Results involve the reduction of the measured CIVλ1549 line width to a VBE (Sect. 4) with a correction factor dependent on both shift amplitude and luminosity. They are discussed in terms of BLR structure (Sect. 5.2), and specifically of the interplay between broadening associated with the outflow (very relevant for CIVλ1549) and with orientation effects (which are dominating for Hβ). Finally, a new $M_{\rm BH}$ scaling law with line width and luminosity (Sect. 5.4) is presented. The new CIVλ1549 scaling law, which considers different corrections for Pop. A and B, separately, may provide an unbiased estimator of black hole masses derived from Hβ over a wide range in luminosity (Sect. 5.5).

2. Sample

2.1. High-luminosity VLT data for Hamburg-ESO quasars

The high-L quasars considered in the present study are 28 sources identified in the HE survey (Wisotzki et al. 2000, hereafter the HE sample) in the redshift range $1.4 \lesssim z \lesssim 3.1$. All satisfy the conditions on the absolute B magnitude $M_{\rm B} \lesssim -27.5$ and on the bolometric luminosity $\log L \gtrsim 10^{47.5}$ erg s^{-1}. They are therefore among the most luminous quasars ever discovered in the Universe, and a relatively rare population even at $z \approx 1-2$ when luminous quasars were more frequent than at low redshift (the luminosity function at $M_{\rm B} \approx -27.5$ is $\Phi(M_{\rm B}) \sim 10^{-8}$ Mpc^{-3} mag^{-1} compared to $\sim 10^{-6}$ Mpc^{-3} mag^{-1} at $M_{\rm B} \approx -25$, corresponding to the "knee" of the Boyle et al. 2000 luminosity function).

The CIVλ1549 data were obtained with the FORS1 spectrograph at VLT and Dolores at TNG; the matching Hβ observations with the ISAAC spectrometer were analyzed in detail by Sulentic et al. (2006a). The resolutions at FWHM of the CIVλ1549 data are $\lesssim$300 km s^{-1} and $\lesssim$600 km s^{-1} for FORS1 and Dolores, respectively; the Hβ resolution is $\approx$300 km s^{-1} (Sulentic et al. 2004). Typical signal-to-noise ratio (S/N) values are $\gtrsim$50.

Resolution and S/N are adequate for a multicomponent nonlinear fitting analysis using the IRAF routine `specfit` (Kriss 1994), involving an accurate deconvolution of Hβ, [OIII]$\lambda\lambda$4959,5007, FeII, HeIIλ4686 in the optical, and of CIVλ1549 and HeIIλ1640 in the UV. The CIVλ1549 and Hβ data and the immediate results of the `specfit` analysis were reported in Paper I.

2.2. Low-luminosity CIVλ1549 and Hβ data

We considered a Faint Object Spectrograph (FOS) sample from Sulentic et al. (2007) as a complementary sample at low-L and low-z. For the sake of the present paper, we restrict the FOS sample to 29 Pop. A and 19 Pop. B RQ (48 in total) sources covering the CIVλ1549 blend spectral range and with previous measurements for the Hβ profile and $R_{\rm FeII}$ (Marziani et al. 2003). The list of sources can be obtained by the cross-correlation of the Sulentic et al. (2007) RQ sources (Kellermann's ratio $\log R_{\rm K} < 1.8$) and the Marziani et al. (2003) catalog on Vizier. We excluded NGC 4395 and NGC 4253 whose luminosities are $\log L \approx 40.4$ and 41.7 [erg s^{-1}], respectively, thus outlying with respect to the L distribution of the FOS sample. The FOS high-resolution grisms yielded an inverse resolution $\lambda/\delta\lambda \sim 1000$, equivalent to typical resolution of the data of Marziani et al. (2003). The S/N is above $\gtrsim$20 for both the optical and UV low-redshift data. The FOS sample has a typical bolometric luminosity $\log L \sim 45.2$ [erg s^{-1}] and a redshift $z \lesssim 0.5$.

2.3. Joint HE+FOS sample

The HE+FOS sample therefore has 76 sources, of which 43 are Pop. A and 33 Pop. B. The distribution of $\log L$ for the 76 sources of the joint sample (derived from the rest-frame luminosity at 1450 Å, assuming a constant bolometric correction equal to 3.5) uniformly covers the range 44–48.5, with similar distributions for Pop. A and B (lower panel of Fig. 1; a K–S test confirms that the two distributions are not significantly different). The Eddington ratio ($L/L_{\rm Edd}$) covers the range 0.01–1 which means complete coverage of the $L/L_{\rm Edd}$ range where most sources in optically selected samples are found.

3. Emission line profile analysis for the FOS+HE sample

3.1. Line modeling and measured parameters

In the following we consider the merit of Hβ and CIVλ1549 as VBEs. Previous work has shown that the Hβ and MgIIλ2800 profiles are almost equally reliable estimators of the "virial" broadening in samples of moderate-to-high luminosity (e.g., Wang et al. 2009; Trakhtenbrot & Netzer 2012; Shen & Liu 2012; Marziani et al. 2013a, excluding the MgIIλ2800 extreme Population A that is significantly broadened by a blueshifted component; Marziani et al. 2013a). However, the broad Hβ line full profile is often affected by asymmetries toward the line base and by significant line centroid shifts. Typically, the Hβ line profiles are characterized by two main asymmetries, differentially

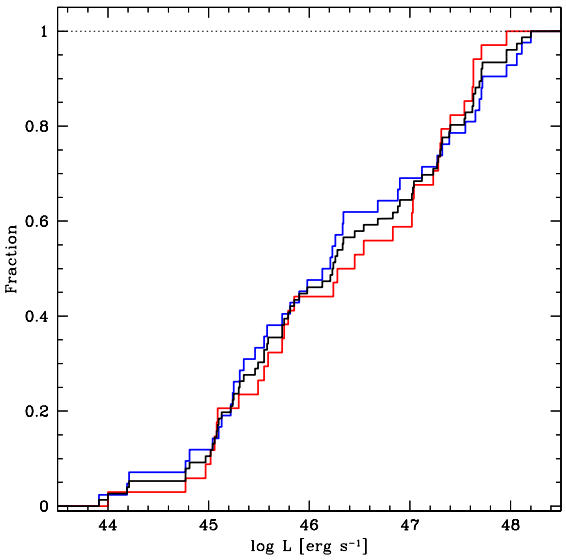

Fig. 1. Cumulative distribution of bolometric luminosity L of the FOS+HE sample (black), Pop. A (blue), and Pop. B (red).

affecting sources in spectral types along the MS (Table A.1 provides the definition of spectral types):

– Pop. A: a blueshifted excess, often modeled with a blueward asymmetric Gaussian component (BLUE) related to the outflows strongly affecting the CIVλ1549 and [OIII]$\lambda\lambda$4959,5007 line profiles (e.g., Negrete et al. 2018, Paper I, and references therein).

– Pop. B: a redward asymmetry modeled with a broader redshifted ($FWHM \sim 10\,000\,\mathrm{km\,s^{-1}}$, $c\left(\frac{1}{2}\right) \sim 2000\,\mathrm{km\,s^{-1}}$) Gaussian. The very broad Gaussian is meant to represent the innermost part of the BLR, providing a simple representation of the radial stratification of the BLR in Pop. B suggested by reverberation mapping (e.g., Snedden & Gaskell 2007). This component (hereafter the very broad component, VBC) has been associated with a physical region of high-ionization virialized and closest to the continuum source (Peterson & Ferland 1986; Brotherton et al. 1994b; Sulentic et al. 2000c; Snedden & Gaskell 2007; Wang & Li 2011). While the properties of the very broad line region (VBLR) remain debatable, a decomposition of the full Hβ profile into a symmetric, unshifted Hβ component (H$\beta_{\rm BC}$) and a H$\beta_{\rm VBC}$ provides an excellent fit to most Hβ Pop. B profiles (Sulentic et al. 2002; Zamfir et al. 2010).

Figures 4 and 5 of Paper I show the Hβ and CIVλ1549 profiles of the HE sample, and their multicomponent interpretation. To extract a symmetric, unshifted component that excludes the blueshifted excess and the VBC, we considered a model of the broad Hβ and CIVλ1549 line with the following components (see also Table A.2):

– Pop. A Hβ and CIVλ1549: an unshifted Lorentzian profile (H$\beta_{\rm BC}$) + one or more asymmetric Gaussians to model the blueward excess (BLUE).

– Pop. B Hβ and CIVλ1549: an unshifted Gaussian (H$\beta_{\rm BC}$) + a redshifted VBC for Hβ (H$\beta_{\rm VBC}$). In the Hβ case, there is no evidence of a blueward excess even at the highest luminosity. However, among Pop. B sources of the HE sample, a prominent CIVλ1549 BLUE appears, implying an intensity ratio CIVλ1549/H$\beta \gg 1$ in the BLUE component. The CIVλ1549 BLUE is usually fainter in the low-luminosity FOS sample Paper I.

In the fits, narrow components of both Hβ (H$\beta_{\rm NC}$) and CIVλ1549 (CIVλ1549$_{\rm NC}$) were included. In the case of CIVλ1549, separation of the broad and narrow component is subject to significant uncertainty, meaning that the effect of the CIVλ1549$_{\rm NC}$ needs to be carefully considered (see discussion in Sect. 3.2).

The decomposition approach summarized above has a heuristic value, as the various components are not defined on the basis of a physical model, even if the assumptions on line shapes follow from MS trends. The distinction between BC and VBC might be physically motivated (the emitting region associated with the BC is the one predominantly emitting FeII), but the decomposition into two symmetric Gaussians is a crude approximation at best. Full profile measurements are added to avoid any exclusive dependence of the results on the profile decomposition. The full profiles of Hβ and CIVλ1549 are parameterized by the FWHM, an asymmetry index (AI), and centroid at $\frac{1}{2}$ and $\frac{1}{4}$ peak fractional intensity, $c\left(\frac{1}{2}\right)$ and $c\left(\frac{1}{4}\right)$. The definition of centroids and AI follows Zamfir et al. (2010):

$$c\left(\frac{i}{4}\right) = \frac{\lambda_{\rm B}\left(\frac{i}{4}\right) + \lambda_{\rm R}\left(\frac{i}{4}\right)}{2\lambda_0} c,\ i = 1, 2, 3;\ \frac{i}{4} = 0.9, \quad (1)$$

$$A.I. = \frac{\lambda_{\rm B}\left(\frac{1}{4}\right) + \lambda_{\rm R}\left(\frac{1}{4}\right) - 2\lambda_{\rm P}}{\lambda_{\rm B}\left(\frac{1}{4}\right) + \lambda_{\rm B}\left(\frac{1}{4}\right)}, \quad (2)$$

where $\lambda_{\rm P}$ is the peak wavelength, and $\lambda_{\rm B}$ and $\lambda_{\rm R}$ are the wavelengths on the blue and red side of the line at the $i/4$ fractional intensities. The centroids are referred to the quasar rest frame, while the AI is referred to as the peak of the line that may be shifted with respect to rest frame. A proxy to $\lambda_{\rm P}$ which is used in this paper is $\tilde{\lambda}_{\rm P} \approx \lambda_0(1 + c(0.9)/c)$.

We assume that the symmetric and unshifted H$\beta_{\rm BC}$ and CIVλ1549$_{\rm BC}$ are the representative line components of the virialized part of the BLR. It is expedient to define a parameter ξ as follows:

$$\xi_{\rm line} = \frac{FWHM_{\rm vir}}{FWHM}, \quad (3)$$

where the $FWHM_{\rm vir}$ is the FWHM of the "virialized" component, in the following assumed to be H$\beta_{\rm BC}$, and the FWHM is the FWHM measured on the full profile (i.e., without correction for asymmetry and shifts). The ξ parameter is a correction factor that can be defined also using components of different lines, for instance CIVλ1549 full profile FWHM and H$\beta_{\rm BC}$, where H$\beta_{\rm BC}$ is assumed to be a reference VBE.

3.2. The CIVλ1549 narrow component in the HE sample and its role in FWHM CIVλ1549$_{\rm BC}$ estimates

In only two cases does CIVλ1549$_{\rm NC}$ contribute to the total CIVλ1549 flux of the HE Pop. B sources by more than 10%: HE2202-2557 and HE2355-4621 (Pop. B, Fig. 5 of Paper I). There is no evidence for a strong NC in the HE Pop. A sources except for HE0109-3518 where I(CIVλ1549$_{\rm NC}$) $\lesssim 0.09$ of the total line flux and whose CIVλ1549 profile resembles those of low-redshift sources that are less luminous by 2–3 dex (the HE0109-3518 CIVλ1549 profile is shown in Fig. 4 of Paper I).

In general, considering H$\beta_{\rm BC}$ as a reference for Pop. B sources, and comparing FWHM H$\beta_{\rm BC}$ to FWHM CIVλ1549 with and without removing the CIVλ1549$_{\rm NC}$ (i.e., to FWHM CIVλ1549$_{\rm BC}$ and FWHM CIVλ1549$_{\rm BC}$ + CIVλ1549$_{\rm NC}$), the CIVλ1549$_{\rm NC}$ removal improves the agreement with FWHM H$\beta_{\rm BC}$ in five out of six cases when CIVλ1549$_{\rm NC}$ has an appreciable effect on the line width (in the other eight cases there is no effect because CIVλ1549$_{\rm NC}$ is too weak). The FWHMs measured

on the CIVλ1549 profiles without removing the CIVλ1549$_{\rm NC}$ (i.e., FWHM CIVλ1549$_{\rm BC}$ + CIVλ1549$_{\rm NC}$) are on average $\approx$−4% and −11 % of the FWHM CIVλ1549, for Pop. A and B, respectively. Therefore, (1) subtracting the CIVλ1549$_{\rm NC}$ improves the agreement between Hβ and CIVλ1549 FWHM; and (2) the average effect is too small to affect our inferences concerning the CIVλ1549 line width as a VBE in the HE sample. The CIVλ1549$_{\rm NC}$ has always been included as an independent component in the line profile fitting of Paper I, following an approach consistently applied to the low-redshift FOS sample and described by Sulentic et al. (2007).

4. Results

4.1. Hβ in the HE sample

We considered several different measurements of the Hβ width following empirical corrections derived from previous work on low-redshift samples:

– Substitution of the H$\beta_{\rm BC}$ extracted through the `specfit` analysis in place of the full Hβ profile.

In principle, extraction of the H$\beta_{\rm BC}$ should be the preferred approach, and the FWHM H$\beta_{\rm BC}$ the preferred VBE. To test the reliability of the FWHM values, we performed Monte-Carlo repetitions of the Hβ fit for Pop. B sources with the broadest lines ($FWHM$ H$\beta_{\rm BC}$ $\sim$ 7000 km s^{-1}, and $FWHM$ H$\beta_{\rm VBC}$ $\sim$ 11 000 km s^{-1}), assuming an $S/N \approx 20$[1], weak and relatively broad [OIII]$\lambda\lambda$4959,5007, a changing noise pattern, and initial values of the fitting. The values of FWHM H$\beta_{\rm BC}$ and H$\beta_{\rm VBC}$ were chosen to represent the broadest lines, where FWHM H$\beta_{\rm BC}$ measurements might be affected by a degeneracy in the BC+VBC decomposition. The dispersion of the Monte Carlo FWHM distribution is almost symmetric, and implies typical FWHM H$\beta_{\rm BC}$ uncertainties $\approx$10% at 1σ confidence level. Therefore, the blending should not be a source of strong bias or of large uncertainties in the H$\beta_{\rm BC}$ and H$\beta_{\rm VBC}$ FWHM[2]. However, we still expect that in the case of very broad profiles, and low S/N or low dispersion, the decomposition of the Hβ profile into H$\beta_{\rm BC}$ and H$\beta_{\rm VBC}$ is subject to large uncertainties that are difficult to quantify. To retrieve information on the H$\beta_{\rm BC}$ we introduce several corrections that can be applied to the full Hβ profile without any multicomponent fitting (which also renders the results model-dependent).

– Symmetrization of the full profile: $FWHM_{\rm symm} = FWHM - -2c\left(\frac{1}{2}\right)$ (`symm` in Fig. 2). The physical explanation behind the symmetrization approach involves an excess radial velocity on the red side that may be due to gas with a radial infall velocity component, with velocity increasing toward the central black hole (e.g., Wang et al. 2017, and references therein). Generally speaking, redward displacements of line profiles have been explained by invoking a radial infall component plus obscuration (Hu et al. 2008; Ferland et al. 2009);

– Substitution of the FWHM H$\beta_{\rm BC}$ with the FWHM measured on the full broad profile of Hβ, corrected according to its spectral type. The spectral types have been assigned following Sulentic et al. (2002, for a conceptually equivalent approach see Shen & Ho 2014). The corrections are as defined from the analysis of the Hβ profile in a large SDSS-based sample at $0.4 \lesssim z \lesssim 0.7$ (labeled as `st` in Fig. 2). In practice, this means to correct Hβ for Pop. B sources by a factor $\xi_{\rm H\beta} \approx 0.8$ (Marziani et al. 2013b) and extreme population A sources ($R_{\rm FeII} \geq 1$) by a factor $\xi_{\rm H\beta} \approx 0.9$. On average, spectral types A1 and A2 show symmetric profiles for which $\xi_{\rm H\beta} \approx 1$. Recent work confirmed that the effect of a blueshifted excess on the full profile of Hβ is small at half-maximum, $0.9 \lesssim \xi_{\rm H\beta} \lesssim 1.0$ (Negrete et al. 2018). We assume $\xi_{\rm H\beta} = 0.9$ as an average correction for ST A3 and A4. The ratio we derive between BC and full profile FWHM of HE Pop. B Hβ is $\approx$0.82 ± 0.09, consistent with the same ratio estimates at moderate luminosity (Marziani et al. 2013b). The `st` correction can be summarized as follows:

ST	$\xi_{\rm H\beta}$
$A3 - A4$	0.9
$A1 - A2$	1.0
$B1 - B1+$	0.8

– Correction of the width of the full broad Hβ profile based on the one derived at low z by pairing the observed full broad Hβ FWHM to the best width estimator from reverberation mapping, following the relation $FWHM_{\rm c} \approx 1.14$ FWHM–601 – 0.0000217FWHM^2 derived by Sulentic et al. (2006a, labeled `corr`);

Figure 2 shows that these corrections all provide similar results if applied to the HE sample FWHM Hβ. Error bars of Fig. 2 were estimated propagating the uncertainty values reported in Paper I for the full profiles, and those derived from `specfit` for the line components (assuming a minimum error of 10%).

The middle panels of Fig. 2 show the ratios of corrected FWHM measurements as a function of the FWHM of the full Hβ profile. The low χ^2_ν indicates that the χ^2_ν associated with the ratios between `BC` and `symm`, and `BC` and `st` is not significantly different from unity. In the case of `BC` and `corr` the two measurements are different but only at 1σ confidence level. The F tests do not exclude that BC, symmetrization, `st`, and reverberation corrections can be equivalent at a confidence level of 2σ. The bottom panel of Fig. 2 shows the behavior of the full and corrected FWHM versus the "symmetrized" Hβ FWHM. We consider the symmetrization, as it is relatively easy to apply (once the quasar rest frame is known), and the `st` correction (that does not even require the knowledge of the rest frame) as reference corrections. We reiterate the fact that these corrections are relatively minor but still significant: a 20% correction translates into a factor 1.44 correction in $M_{\rm BH}$. They do not undermine the value of the full line width of Hβ as a useful VBE (with the caveats discussed in Sect. 5.2), since the Hβ full line width remains preferable to the uncorrected CIVλ1549 width for most objects.

4.2. CIVλ1549 in the full HE+FOS sample

The results on the HE CIVλ1549 profiles do not bode well for the use of CIVλ1549 FWHM as a VBE, as also found by Sulentic et al. (2007) and other workers (Sect. 5.1 for a brief critical review). The presence of very large blueshifts in both Pop. A and B makes the situation even more critical than at low L. Figure 3 (top panel) shows that there is no obvious relation between the FWHM of CIVλ1549 and the FWHM of Hβ if FOS+HE data are considered together.

For the Pop. A sources in the HE+FOS sample, CIVλ1549 is broader than Hβ, apart from in two cases in the HE sample, and FWHM(CIVλ1549) shows a broad range of values for similar FWHM Hβ, that is, FWHM(CIVλ1549) is almost degenerate

[1] S/N is measured per pixel on the continuum.

[2] If S/N is relatively high ($\gtrsim$20) only in some peculiar cases might the uncertainty be significantly larger. For example, if the Hβ profile is composed for a narrower core and a broader base, the FWHM measure is unstable, and may abruptly change depending on continuum placement.

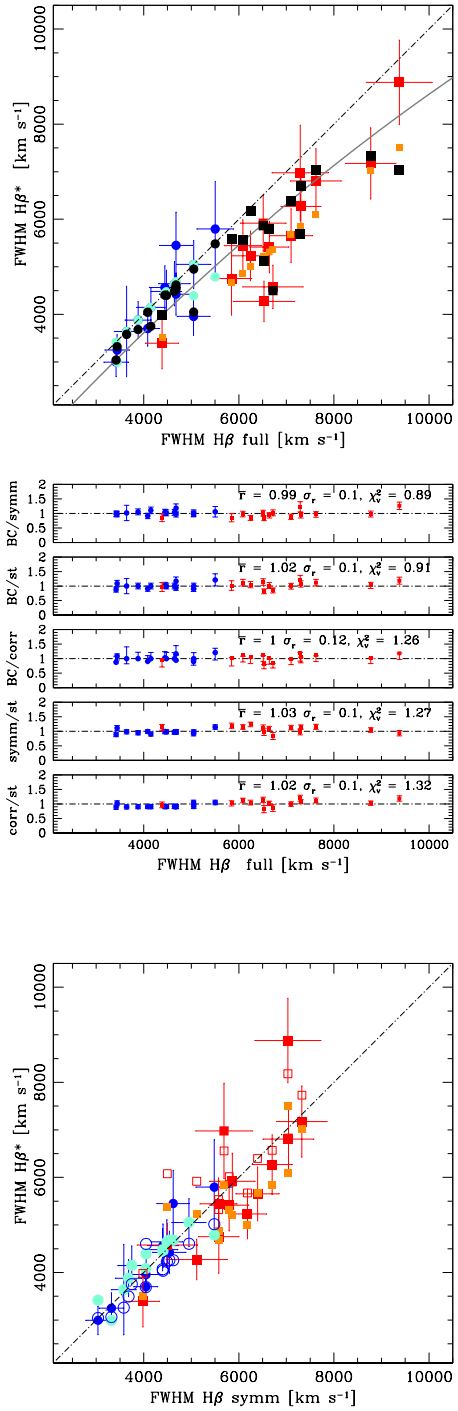

Fig. 2. Virial broadening estimators based on Hβ, with several corrections applied to the HE sample. *Top square panel*: FWHM H$\beta_{\rm BC}$ (blue (Pop. A) and red (Pop. B)) with error bars, symmetrized FWHM Hβ (`symm`, black), and FWHM Hβ corrected according to spectral type (`st`, aquamarine and dark orange for Pop. A and B respectively) versus FWHM of the full Hβ profile. The gray line traces the correction (`corr`) following the relation of Sulentic et al. (2006a) reported in Sect. 4. *Middle panels*: ratios of FWHM after various corrections vs. full profile FWHM. Panels from top show: BC/`symm`, BC/`st`, BC/`corr`, `symm`/`st`, `corr`/`st`. Average values, standard deviation and normalized χ^2_ν are reported in the upper-right corner of the panels. *Bottom square panel*: BC, spectral type `st` and reverberation corrected (`corr`, open symbols) FWHM values vs. symmetrized FWHM.

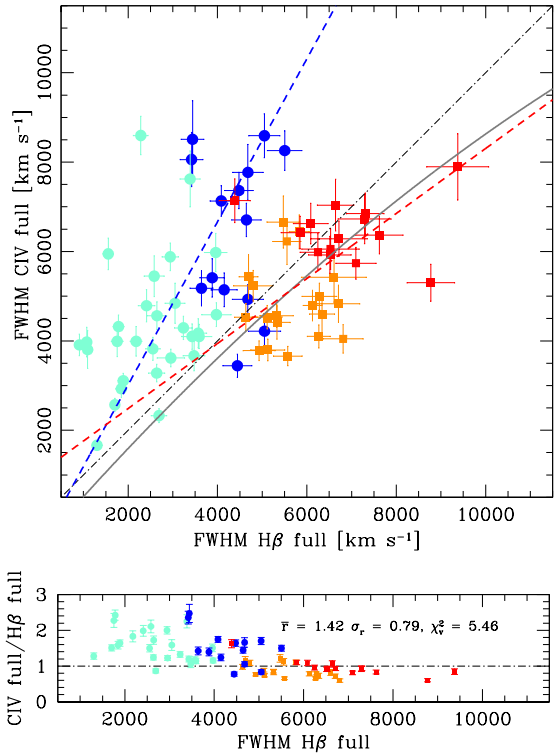

Fig. 3. *Top panel*: FWHM(C IVλ1549) vs. FWHM(Hβ) (full profiles) for the FOS+HE sample. Data points are color-coded according to sample and population: HE Pop. A – blue circles (●), HE Pop. B – red squares (■), FOS Pop. A – aquamarine circles (●), and FOS Pop. B – golden squares (■). Best fitting least-square lines (dashed) are shown in blue for all Pop. A and red for all Pop. B. The black dot-dashed line is the equality line. The continuous gray line is the expected FWHM following the correction of Sulentic et al. (2006a, `corr`). *Lower panel*: ratio between FWHM C IVλ1549 and FWHM Hβ as a function of FWHM (Hβ).

with respect to Hβ. The C IVλ1549 line FWHM values are so much larger than the ones of Hβ, thus making it possible that the $M_{\rm BH}$ derived from FWHM C IVλ1549 might be higher by even more than one order of magnitude. Formally, the Pearson's correlation coefficient $r \approx 0.52$ is highly significant for a sample of $n = 43$, with significance at a confidence level $\approx 4.5\sigma$. A weighted least-square fit yields $FWHM(\text{C IV}\lambda1549) = (1.822 \pm 0.204) FWHM(\text{H}\beta) + (-624 \pm 677)$ km s^{-1}, with a significant scatter, rms ≈ 1959 km s^{-1}. Unfortunately it is not possible to apply a simple C IVλ1549 symmetrization as done for Hβ: subtracting $2 \cdot c\left(\frac{1}{2}\right)$ from FWHM C IVλ1549 leads to corrections that are unrealistically large.

If we combine the Pop. B FOS and HE samples, FWHM C IVλ1549 and Hβ become loosely correlated (the Pearson's correlation coefficient is $\approx$0.4, significant at $P \approx 98\%$ for a sample of 33 objects). A weighted least-square fit yields $FWHM(\text{C IV}\lambda1549) \approx (0.764 \pm 0.165) FWHM(\text{H}\beta) + (810 \pm 1030)$ km s^{-1}, and rms $\approx$ 1090 km s^{-1}, with a significant deviation from the 1:1 relation. In the case of Pop. B sources, the trend implies FWHM C IVλ1549 $\sim$ FWHM Hβ, and even a slightly narrower FWHM C IVλ1549 with respect to Hβ.

The large scatter induced by using an uncorrected C IVλ1549 line FWHM may have contributed to the conclusion that line width does not contribute significantly to $M_{\rm BH}$ determinations (Croom 2011).

4.3. Practical usability of C IVλ1549$_{\rm BC}$

The fitting procedure scaled the Hβ profile to model the red side of C IVλ1549 meaning that the FWHM C IVλ1549$_{\rm BC}$ estimate

is not independent from FWHM Hβ_{BC}. The FWHM values of the two BCs are in agreement because of this enforced condition.

The CIVλ1549$_{BC}$ extraction is very sensitive to the assumed rest frame, and also requires that the CIVλ1549 line be cleaned from contaminants such as FeII (weak) and HeIIλ1640 (moderate, but flat-topped and gently merging with the CIVλ1549 red wing; Marziani et al. 2010; Fine et al. 2010; Sun et al. 2018). Without performing a line profile decomposition, one can consider the width of the red side with respect to rest frame as the half width at half maximum (HWHM) of the virial component. Again this requires (1) an accurate redshift that can be set, in the context of high-redshift quasars, either by using the Hβ narrow component or by the [OII]λ3727 doublet (Eracleous & Halpern 2004; Hu et al. 2008), and (2) the decomposition from HeIIλ1640 emission blended on the CIVλ1549 red side. If [OII]λ3727 is covered, then MgIIλ2800 is also likely to be covered. As mentioned in Sect. 3, the MgIIλ2800 line width is a reliable VBE for the vast majority of type-1 AGNs. The same is not true for CIVλ1549. For spectra where CIVλ1549 is conveniently placed at $z \gtrsim 1.45$, the [OII]λ3727 line is shifted beyond 9000 Å, a domain where intense sky emission makes it difficult to analyze a relatively faint narrow line. The extraction of CIVλ1549$_{BC}$ is therefore not a viable solution if single-epoch CIVλ1549 observations are available without the support of at least a narrow LIL that may set a reliable rest frame. This is unlikely to occur on the same optical spectra. An alternative strategy for M_{BH} estimation using CIVλ1549 FWHM should consider the origin of the CIVλ1549 nonvirial broadening.

4.4. Reducing CIVλ1549 to a VBE estimator consistent with Hβ

The main results of Paper I suggest a strong dependence of the CIVλ1549 blueshift on L/L_{Edd}, especially above a threshold value $L/L_{Edd} \approx 0.2 \pm 0.1$ (Sulentic et al. 2014, and references therein). A correlation between Eddington ratio and the FWHM(CIVλ1549) to FWHM(Hβ) ratio (i.e., $1/\xi_{CIV}$, cf., Saito et al. 2016) is detected at a high significance level (Pearson's correlation coefficient $r \approx 0.55$) joining all FOS RQ sources of Sulentic et al. (2007; Fig. 4). In this context, L/L_{Edd} was computed from the M_{BH} scaling law of Vestergaard & Peterson (2006) using the FWHM of Hβ and λL_λ(5100). A bisector best fit with SLOPES (Feigelson & Babu 1992) yields

$$\log \frac{1}{\xi_{CIV}} \approx (0.426 \pm 0.043)\frac{L}{L_{Edd}} + (0.401 \pm 0.035). \quad (4)$$

An L/L_{Edd}-dependent correction is in principle a valid approach. However, how to calculate L/L_{Edd} from UV spectra without resorting to Hβ observations is not obvious. In addition, FWHM Hβ is strongly affected by orientation and yields biased values of L/L_{Edd} (Sect. 5.2.2). Both FWHM(Hβ_{BC})/FWHM(CIVλ1549) and $c\left(\frac{1}{2}\right)$ are correlated with Eddington ratio. Consistently, the CIVλ1549 blueshift is correlated with FWHM CIVλ1549 (Paper I, Coatman et al. 2016), and accounts for the broadening excess in the CIVλ1549 FWHM. Measurements of the CIVλ1549 blueshift or the FWHM(Hβ_{BC})/FWHM(CIVλ1549) can be used as proxies for L/L_{Edd}. At the same time, Paper I reveals a weaker correlation with L, which is expected in the case of a radiation-driven wind. If the correction factor is $\xi_{CIV} = FWHM(H\beta_{BC})/FWHM(CIV\lambda1549)$, then it should include a term in the form $1/\zeta(L, L/L_{Edd})$.

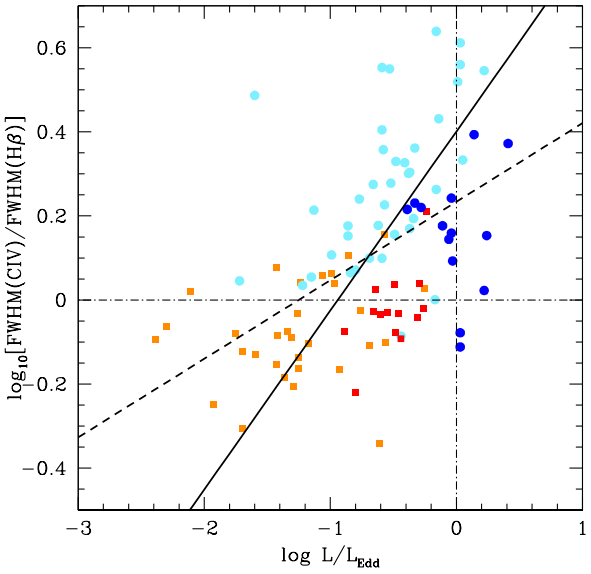

Fig. 4. Relation between the logarithm of the FWHM ratio of CIVλ1549 to Hβ and the logarithm of the Eddington ratio L/L_{Edd}. The vertical dot-dashed line traces the Eddington limit. The colors and shapes of symbols are as in Fig. 3. The dashed line is an unweighted least-squares fit, and the filled line was obtained with the bisector method (Feigelson & Babu 1992).

4.5. Calibrating empirical corrections on FWHM CIVλ1549

Coatman et al. (2017) introduced a nonparametric measurement of the CIVλ1549 blueshift associated with the wavelength that splits the line flux in equal parts on its blue and red sides (flux bisector). The flux bisector is strongly correlated with $c\left(\frac{1}{2}\right)$ and $c\left(\frac{1}{4}\right)$, and $c\left(\frac{1}{2}\right)$ and $c\left(\frac{1}{4}\right)$ are correlated among themselves in the FOS+HE sample (Pearson's $r \approx 0.95$): $c\left(\frac{1}{2}\right) = (0.773 \pm 0.307)c\left(\frac{1}{4}\right) - (58 \pm 65)$ km s^{-1}. The bisector correlation is stronger with $c\left(\frac{1}{4}\right)$ (Pearson's correlation coefficient $r \approx 0.98$), with flux bisector $\sim(0.98 \pm 0.04)c\left(\frac{1}{4}\right) + (220 \pm 110)$ km s^{-1} (Fig. 5). The lower panel of Fig. 5 shows a few objects where the difference between the $c\left(\frac{1}{4}\right)$ and the flux bisector is $\gtrsim$20%; these sources are either with small shifts (within the measurement uncertainties; shaded area of Fig. 5), or sources strongly affected by broad absorptions, for which measurement of blueshift is tricky regardless of the method employed. Therefore, it is possible to apply Eq. (4) of Coatman et al. (2017) substituting the $c\left(\frac{1}{4}\right)$ to the flux-bisector blueshift measurements:

$$\xi_{CIV,0} = \frac{1}{a\left(-\frac{c\left(\frac{1}{4}\right)}{1000}\right) + b}, \quad (5)$$

with $a = 0.41 \pm 0.02$ and $b \approx 0.62 \pm 0.04$ (the minus sign is because Coatman et al. (2017) assumed blueshifts to be positive), to correct the FWHM CIVλ1549 of the FOS+HE sample. The resulting trend is shown in Fig. 6. Equation (4) of Coatman et al. (2017) undercorrects both Pop. A and B sources at low L (the FOS sample) and provides a slight overcorrection for the HE sources. The correction of Coatman et al. (2017) does not yield FWHM (CIVλ1549) in agreement with the observed values of FWHM(Hβ). This does not necessarily mean that the FWHM(CIVλ1549) values are incorrect, as FWHM(Hβ) is likely more strongly affected by orientation effects than FWHM(CIVλ1549); see the discussion in Sect. 5.2.

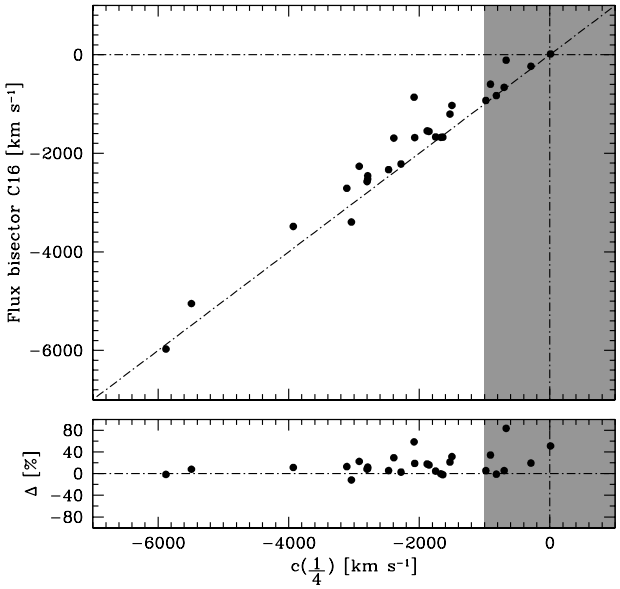

Fig. 5. *Top panel*: bisector flux estimator of Coatman et al. (2017) vs. $c\left(\frac{1}{4}\right)$, in km s^{-1}. The dot-dashed line is the equality line. *Bottom panel*: percentage residuals. The shaded areas indicate the average errors of measurements at a 2σ confidence level computed from Table 4 of Paper I.

A correction dependent on luminosity reduces the systematic differences between the various samples in the present work but it has to be separately defined for Pop. A and B (Fig. 7). The following expression provides a suitable fitting law, with a, b, c different for Pop. A and B.

$$\xi_{\rm CIV,1} = \frac{1}{b\,(a - \log \lambda L_\lambda(1450)) \cdot \left(\left|\frac{c\left(\frac{1}{2}\right)}{1000}\right|\right) + c}. \quad (6)$$

Here we consider the $c\left(\frac{1}{2}\right)$ because of its immediate connection with the FWHM, and because it is highly correlated with $c\left(\frac{1}{4}\right)$ (Sect. 5.5). Equation (6) is empirical: it entails a term proportional to shift and one to the product of $\log L_{1450}$ and shift. Multivariate, nonlinear lsq results for Eq. (6) are reported in the first rows of Table 1. For Pop. A, the correction is rather similar to the one of Coatman et al. (2017), and is driven by the large blueshifts observed at high $L/L_{\rm Edd}$. The luminosity-dependent factor accounts for low-luminosity sources that are not present in the Coatman et al. (2017) sample. The use of the absolute value operator provides an improvement with respect to the case in which blueshifts are left negative. There are only three objects for which $c\left(\frac{1}{2}\right)$ is positive. The improvement is understandable if one considers any CIVλ1549 shift as affecting the difference between the FWHM of CIVλ1549 and Hβ. An A(+) sample was defined from the Pop. A sample minus three objects with positive $c\left(\frac{1}{2}\right)$, that is, all A(+) sample sources show blueshifts. No significant improvement was found with respect to the previous sample.

The correction for Pop. B is less well defined, considering the uncertainty in a, and the low value of b (Table 1). The corrections for Pop. B still offer an improvement because they remove significant bias (as evident by comparing Figs. 3 and 7). In practice, for Pop. B, at low L the $\xi_{\rm CIV}$ could be considered constant to a zero-order approximation, with $\xi_{\rm CIV} \sim 1$. In other words, when the velocity field is predominantly virial, and no prominent blueshifted component affects the line width, CIVλ1549 may be somewhat broader than Hβ as expected for the stratification revealed by reverberation mapping of lines from different ionic species (Peterson & Wandel 1999, 2000). The fit is consistent with $\xi_{\rm CIV}$ depending on shift but only weakly on luminosity. The Pop. B correction is so ill-defined that larger samples are needed for a better determination of its coefficients.

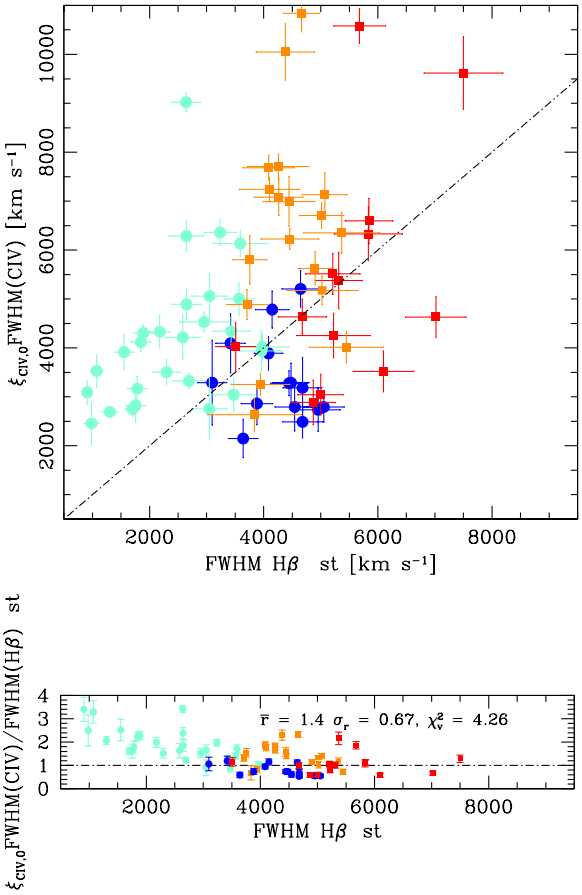

Fig. 6. *Top panel*: FWHM(CIVλ1549) `C16` (i.e., corrected following Coatman et al. 2016), vs. FWHM(Hβ) `st` for the FOS+HE sample. Meaning of symbols is the same as for Fig. 3. The black dot-dashed line is the equality line. *Bottom panel*: residuals. Average ratio, dispersion, and χ^2_ν refer to all sources.

Slightly different fitting laws

$$\xi_{\rm CIV,2} = \frac{1}{a + b \log \lambda L_\lambda(1450) + c\frac{c\left(\frac{1}{2}\right)}{1000}}, \quad (7)$$

which considers a linear combination $\log \lambda L_\lambda(1450)$ and shift, and

$$\xi_{\rm CIV,3} = \frac{1}{a - b \log \lambda L_\lambda(1450) \cdot \frac{c\left(\frac{1}{2}\right)}{1000}}, \quad (8)$$

which assumes a dependence from the product $\log \lambda L_\lambda(1450)$ and shift, provide consistent results, with fitting parameters, 1σ confidence level associated uncertainty, and root mean square (rms) residuals of $\xi_{\rm CIV}$ reported in Table 1. The fitting relations yield a lower residual scatter in $\xi_{\rm CIV}$ than assuming no luminosity dependence. For instance, using Eq. (7) we obtain a scatter in $\xi_{\rm CIV,2}$ that is a factor 1.86 lower than if Eq. (5) is used. We also considered the AI in place of $c\left(\frac{1}{2}\right)$ in Eq. (6) (without the absolute value operator; bottom rows of Table 1). The AI has a

Table 1. Fits of $\xi_{\rm CIV}$.

Sample	$a \pm \delta a$	$b \pm \delta b$	$c \pm \delta c$	rms_ξ	d.o.f.
$\xi_{\rm CIV,1} \approx 1/(b*(a-x)*\lvert y\rvert + c)$					
A	−0.3093 0.1581	0.3434 0.0881	1.0763 0.0949	0.198	40
B	3.9224 14.1170	0.0206 0.0568	0.9845 0.0602	0.187	30
A+B	−0.1805 0.2603	0.1978 0.0584	1.0117 0.0641	0.227	73
$\xi_{\rm CIV,1} \approx 1/(b*(a-x)*y + c)$					
A	−0.4161 0.3325	−0.1825 0.0693	1.3245 0.0919	0.222	40
B	28.967 496.591	−0.0030 0.0486	1.0182 0.0449	0.187	30
A+B	−0.1346 0.4991	−0.1202 0.0467	1.1508 0.0510	0.238	73
$\xi_{\rm CIV,2} \approx 1/(a + b*x + c*y)$					
A	0.356 0.160	−0.3480 0.0580	−0.351 0.0814	0.199	40
B	1.080 0.126	0.0223 0.0416	−0.0764 0.0515	0.186	30
A+B	0.7605 0.125	−0.1460 0.0452	−0.2204 0.0532	0.237	73
$\xi_{\rm CIV,3} \approx 1/(a - b*x*y)$					
A	1.3036 0.0884	−0.1408 0.0481	...	0.222	41
B	1.0343 0.0436	−0.0463 0.0255	...	0.187	31
A+B	1.1470 0.0488	−0.1116 0.0288	...	0.237	74
$\xi_{\rm CIV,AI} \approx 1/(b*(a-x)*z + c)$					
A	−1.7004 0.5528	−1.0575 0.4703	1.5515 0.1183	0.240	40
B	−2.346 0.3153	0.7571 0.3026	1.1057 0.0413	0.184	30
A+B	5.147 21.138	−0.1121 0.3292	1.2474 0.0501	0.257	73

Notes. $x = \log \lambda L_\lambda(1450) - 48$, for $\log \lambda L_\lambda(1450) \lesssim 47.5$ [ergs^{-1}]; $y = c\left(\frac{1}{2}\right)/1000$, z = AI.

non-negligible advantage to be independent from the choice of the rest frame. The AI is correlated with both $c\left(\frac{1}{4}\right)$ and $c\left(\frac{1}{2}\right)$, and shows higher correlation with $c\left(\frac{1}{4}\right)$ (Pearson's $r \approx 0.66$). However, the scatter in $\xi_{\rm CIV,A.I.}$ is unfortunately large, and would imply a scatter ≈1.5 higher in $M_{\rm BH}$ estimates than in the case where Eq. (6) is considered for Pop. A.

If Pop. A and B are considered together, the final scatter in $\xi_{\rm CIV}$ is close for the different fitting function (Eq. (6) yields a slightly better result) but much higher than if Pop. A and B are kept separated. It is therefore necessary to distinguish between Pop. A and B as the intrinsic structure of their BLR may be different (e.g., Goad & Korista 2014; Wang et al. 2014a). In Pop. B, at low $L/L_{\rm Edd}$, the lines are mainly broadened following a virial velocity field (Peterson & Wandel 2000). The relative prominence of the blueshifted to the virialized component (ratio BLUE over BC) is lower in Pop. B than in Pop. A, a consequence of the low $L/L_{\rm Edd}$ for Pop. B sources. Both properties are expected to contribute to the overall consistency between Hβ and CIVλ1549 profiles in Pop. B sources. At any rate, $\xi_{\rm CIV}$ should always be $\lesssim$1, with $\xi_{\rm CIV} \approx 1$ for Pop. B at low L, and $\xi_{\rm CIV} \ll 1$ in case of very large shifts, as in Pop. A at high L.

It is possible in most cases to distinguish between Pop. A and B from the UV spectrum emission blend, making the correction applicable at least to a fraction of all quasars in large samples. Several criteria were laid out by Negrete et al. (2014): (1) broad line width; (2) evidence of a prominent red wing indicative of a VBC; and (3) prominence of CIII]λ1909. Population B sources show a CIVλ1549 red wing and strong CIII]λ1909 in the 1900 Å. Extreme Pop. A (xA) sources are easy to recognize; they show strong AlIIIλ1860 in 1900 Å blend and low W(CIVλ1549). A prototypical composite spectrum of xA sources is shown by Martínez-Aldama et al. (2018). However, some intermediate cases along the MS (i.e., spectral type A1) may be easier to misclassify. Also, with only the UV spectral range available, the redshift estimate may be subject to large errors. Negrete et al. (2014) provide a helpful recipe; however, their recipe applied to three of their eight sources allowed for a precision of ∼100 km s^{-1} in the rest frame, but the remaining five had an average uncertainty $\gtrsim$500 km s^{-1}.

5. Discussion

Recently, the problems outlined in earlier works by Sulentic et al. (2007) and Netzer et al. (2007) have been ascribed to a "bias" in the CIVλ1549 $M_{\rm BH}$ estimates (Denney et al. 2016). The CIVλ1549 $M_{\rm BH}$ bias is dependent on the location in the 4DE1 quasar MS: Figs. 2 and 3 clearly show the different behavior for Populations A and B. By the same token, an $L/L_{\rm Edd}$-dependent correction is in principle a valid approach, as $L/L_{\rm Edd}$ is probably one of the main drivers of the MS (Boroson & Green 1992; Sulentic et al. 2000a; Sun & Shen 2015). Unfortunately, several recent works still ignore 4DE1-related effects (or, in other words, MS trends). For instance, scaling laws derived from the pairing of the virial products for all sources with reverberation mapping data should be viewed with care (as shown by the reverberation mapping results of Du et al. 2018).

5.1. CIVλ1549 and Hβ as $M_{\rm BH}$ estimators: input from recent works

Attempts at using the CIVλ1549 as a VBE have been renewed in the last few years, not least because CIVλ1549 can be observed in the optical and NIR spectral ranges over which high-redshift quasars have been discovered and are expected to be discovered in the near future. The large CIVλ1549 blueshifts indicate that part of the BLR gas is under dynamical conditions that are far from virialized equilibrium. At high Eddington ratios, ionized gas may escape from the galactic bulge, and even be dispersed into the intergalactic medium, as predicted by numerical simulations (e.g., Debuhr et al. 2012), and at high luminosity

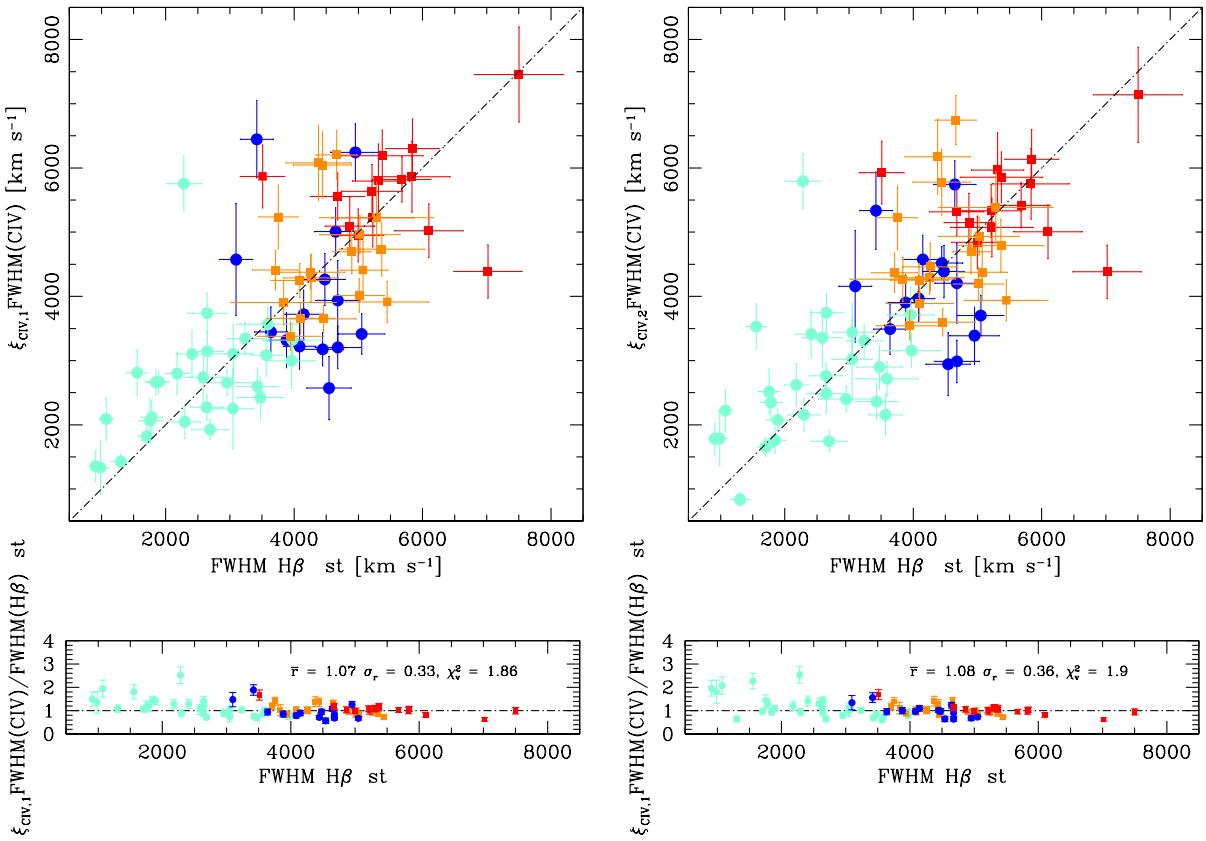

Fig. 7. *Top left panel*: $\xi_{\rm CIV}$FWHM(Civλ1549) i.e., FWHM(Civλ1549) after correction for blueshift and luminosity dependence following Eq. (6) vs. FWHM(Hβ) cm for the FOS+HE sample. The black dot-dashed line is the equality line, and the meaning of the color-coding is the same as in Fig. 3. *Top right*: as in top panel but with $\xi_{\rm CIV}$ computed from Eq. (7).

($\log L \gtrsim 47\,[{\rm erg\,s^{-1}}]$) they might have a significant feedback effect on the host galaxy (Marziani et al. 2016).

A firm premise is that the disagreement between Hβ and Civλ1549 mass estimates is not a matter of S/N (Denney et al. 2013). The Civλ1549 line width suffers from systematic effects which emerge more dramatically at high S/N, i.e., when it is possible to appreciate the complexity of the Civλ1549 profile. Given this basic result, recent literature can be tentatively grouped into three main strands: (1) low-redshift studies involving FOS and Cosmic Origin Spectrograph (COS) spectra to cover Civλ1549; (2) high-redshift studies, where the prevalence of large Civλ1549 shifts is high; and (3) studies attempting to correct the Civλ1549 FWHM and reduce it to an equivalent of Hβ, some of them employing results that are directly connected to the MS contextualization of quasar properties.

Low-redshift studies. A large systematic analysis of the Civλ1549 profiles paired to Hβ emission was carried out using HST/FOS (in part used for the present work) and optical observations (Sulentic et al. 2007). The results of this study emphasized the role of the Civλ1549 line width in the $M_{\rm BH}$ estimates. Figure 6 of Sulentic et al. (2007) clearly shows the importance of placing sources in an E1 context: estimates of the masses could be easily overestimated by a factor $\lesssim$100 for extreme Pop. A sources such as I Zw 1, while for Pop. B, Civλ1549 and Hβ $M_{\rm BH}$ estimates appeared more consistent albeit with a large scatter. The line width (be it the FWHM or the velocity dispersion σ) remains a major factor in Civλ1549 versus Hβ $M_{\rm BH}$ determinations since broadening enters squared in the scaling laws (Kelly & Bechtold 2007). Similar warnings on using Civλ1549 FWHM were issued by Netzer et al. (2007). Low-redshift samples are less affected by the Eddington ratio bias that is cutting low-Eddington ratio sources at a given $M_{\rm BH}$ for a fixed flux limit (Sulentic et al. 2014). Therefore, it may not be surprising to find studies based on excellent spectra that find an overall consistency between Hβ and Civλ1549 $M_{\rm BH}$ estimates. Intrinsic scatter is probably high if full line widths without corrections are used: Tilton & Shull (2013) find $\approx$0.5 dex from COS observations of low-redshift quasars. Denney et al. (2013) claim to be able to reduce the disagreement between $M_{\rm BH}$ derived using Hβ and Civλ1549 to $\approx$0.24 dex by using the velocity dispersion of the Civλ1549 line. Since the Civλ1549 profile in the Denney et al. (2013) sample almost never shows large blueshifts, which may be associated to a velocity shear in outflowing gas, these results appear consistent with the Pop. B properties of the FOS sample.

High-redshift studies. These studies generally agree on the fact that the Civλ1549 FWHM is poorly correlated with the Balmer line FWHM. Shen & Liu (2012) describe the scatter between Civλ1549 and Hβ FWHM as due to an irreducible part ($\approx$0.12 dex), and a part that correlates with the blueshift of the Civλ1549 centroid relative to that of Hβ. These latter authors propose scaling laws in which the virial assumption is abandoned, that is, with the exponent of the line FWHM being significantly different from two. For Civλ1549, this means correcting for the overbroadening associated with the nonvirial component. The scaling law introduced by Park et al. (2013) is consistent with the approach by Shen & Liu (2012) and implies $M_{\rm BH} \propto FWHM^{0.5}$, that is, a FWHM dependence that is very different from the one expected from a virial law ($M_{\rm BH} \propto FWHM^2$). As shown in Fig. 8, the scaling law suggested by Park et al. (2013) applied to the HE sample properly corrects for the

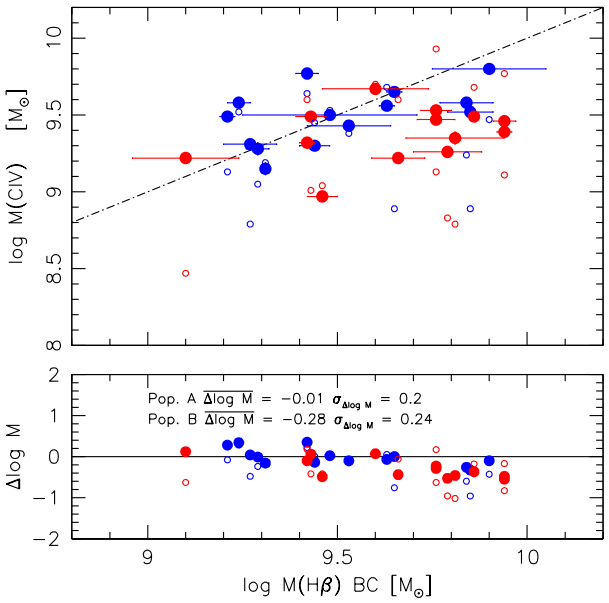

Fig. 8. Black hole mass computed from the fiducial relation of Vestergaard & Peterson (2006) based on FWHM Hβ vs. the ones computed from the CIVλ1549 FWHM following Park et al. (2013), for Pop. A (blue) and B (red) HE sources. Values of $M_{\rm BH}$ obtained from the Vestergaard & Peterson (2006) CIVλ1549 scaling law after the correction suggested by Brotherton et al. (2015, small dots) are shown by small open circles. *Lower panel*: residuals as a function of $M_{\rm BH}$. The average and the scatter reported for Populations A and B refer to the Park et al. (2013) scaling laws.

overbroadening of Pop. A sources, but overcorrects the width of Pop. B, yielding a large deviation from the Hβ-derived $M_{\rm BH}$ values (on average ≈0.28 dex).

Studies exploiting MS trends. The results reported in Sect. 4 and in Paper I indicate that any solution seeking to bring CIVλ1549 $M_{\rm BH}$ estimates into agreement with the ones from Hβ cannot exclude the strong $L/L_{\rm Edd}$ dependence of the CIVλ1549 blueshift that is in turn affecting the CIVλ1549 FWHM (Fig. 4). The discussion in Sects. 3 and 4.5 here identifies the CIVλ1549 blueshift as an expedient $L/L_{\rm Edd}$ proxy. Any parameterization of the blueshifted amplitude such as $c\left(\frac{1}{2}\right)$, the flux bisector of Coatman et al. (2016), or the ratio FWHM(CIVλ1549)/FWHM(Hβ) takes into account the MS trends in CIVλ1549 properties due to the $L/L_{\rm Edd}$ and CIVλ1549 blueshift correlation. Another $L/L_{\rm Edd}$ proxy may involve the SiIVλ1397/CIVλ1549 peak ratio: at low SiIVλ1397/CIVλ1549 the $M_{\rm BH}$ is underestimated with respect to Hβ, and at high SiIVλ1397/CIVλ1549 the mass is overestimated (Brotherton et al. 2015). Since the ratio SiIVλ1397/CIVλ1549 is a known 4DE1 correlate (Wills et al. 1993; Bachev et al. 2004), these results confirm that FWHM CIVλ1549 leads to an overestimate of $M_{\rm BH}$ for Pop. A (as Pop. A outflows produce blueshifted emission that significantly broadens the line (Fig. 3; cf. Denney et al. 2012). In our sample, however, applying the correction suggested by Brotherton et al. (2015), that is, $\delta \log M \approx -1.23 \log \frac{1400}{\rm CIV} - 0.91$, to the masses derived from the Park et al. (2013) would move the $M_{\rm BH}$ of Pop. B further down, leading to a further increase of the overcorrection, and also destroying the agreement for Pop. A sources; on top of the $\propto FWHM^{0.5}$ law, the additional correction is $\delta \log M \approx -0.91$ if $\frac{1400}{\rm CIV} \sim 1$. The correction is lower but still negative for most Pop. B sources where $\frac{1400}{\rm CIV} \sim 0.3$, exacerbating the disagreement between the Hβ and CIVλ1549 derived masses. Better consistency is achieved if the correction of Brotherton et al. (2015) is applied to the Vestergaard & Peterson (2006) scaling law for CIVλ1549. In this case (shown in Fig. 8 by small open circles) the correction for Pop. A still implies non-negligible systematic residuals $\delta \log M = \log M_{\rm BH}({\rm H}\beta_{\rm BC}) - \log M_{\rm BH}({\rm CIV}\lambda 1549) \approx 0.23$. The average residual is higher for Pop. B $M_{\rm BH}$, with $\delta \log M \approx 0.27$, and scatter ≈0.39 dex.

Assef et al. (2011) used a sample of approximately ten sources with optical spectra covering CIVλ1549 and NIR spectra covering Hβ or Hα and showed that $M_{\rm BH}$ estimates can be made consistently. The approach of Assef et al. (2011) may also be understood as a correction related to the MS. Assef et al. (2011) suggest that much of the dispersion in their virial mass is caused by the poor correlation between λL_λ at 5100 Å and at 1350 Å rather than between their line widths. Their Figs. 14 and 15 show that the FWHM CIVλ1549 to Hβ ratio depends on the flux ratio at 1350 Å and 5100 Å, which is an MS correlate (Laor et al. 1997; Shang et al. 2011). The Assef et al. 2011 sample of gravitationally lensed quasars might have lowered the Eddington ratio bias described by Sulentic et al. (2014), leading to a preferential section of Pop. B quasars, and better agreement between Hβ and CIVλ1549 line width.

5.2. A virialized component

5.2.1. Similar Hβ and CIVλ1549 luminosity trends

A systematic increase in line width in the HE sample is expected if the line broadening is predominantly virial: Fig. 5 of Paper I shows that there are no FWHM H$\beta \lesssim 3000\,{\rm km\,s^{-1}}$ at $\log L \gtrsim 47\,[{\rm erg\,s^{-1}}]$. Figure 9 here shows that a similar increase in FWHM as a function of luminosity is occurring in the FOS+HE sample for both Hβ and CIVλ1549. The FWHM ratio between CIVλ1549 and Hβ does not instead appear strongly influenced by L, leading to the interpretation that the broadening of both lines – even if the CIVλ1549 centroid measurements are significantly affected by an outflowing component – may be mostly related to the gravitational effects of the supermassive black hole (as further discussed below). As mentioned, Balmer lines provide a VBE up $z \gtrsim 2$, and the results of Paper I extended this finding to the highest luminosities. For CIVλ1549, Fig. 9 and the correlation $FWHM - c\left(\frac{1}{2}\right)$ justify the assumption of a virial broadening component coexisting with a nonvirial one (Wang et al. 2011).

5.2.2. Orientation effects on Hβ

A large part of the CIVλ1549 – Hβ scatter is expected to be due to orientation effects. The issue of orientation effects remains open for RQ sources, and orientation effects are most likely strongly affecting the FWHM of Hβ (Mejía-Restrepo et al. 2018b), even if it remains hard to distinguish them from other physical factors (such as $M_{\rm BH}$ and $L/L_{\rm Edd}$). A clue is given by the 4DE1 predictions at extreme orientations: objects observed near the disk rotation axis (i.e., nearly pole-on) have the smallest FWHM Hβ, the strongest FeII and CaII intensities (Dultzin-Hacyan et al. 1999), the largest soft X excess, and the largest CIVλ1549 blue shifts/asymmetries. These predictions are motivated by the physical scenarios involving an accretion disk–wind system. From a pole-on orientation we should see the smallest Doppler broadening of virially dominated Hβ-emitting clouds, and the strongest intensity of FeII and other LILs if they are emitted from clouds in the outer part of the disk (Martínez-Aldama et al. 2015). We should also observe the largest contribution of the soft X excess if it is related to disk emission (Wang et al. 1996, 2014b; Boller et al. 1996). Finally, if a wind is associated with an optically

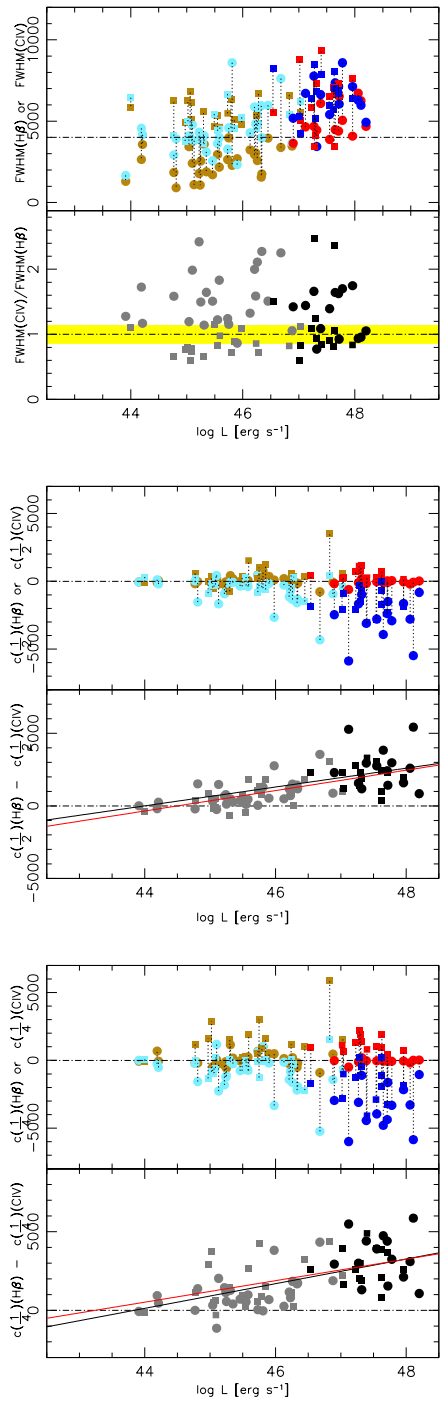

Fig. 9. Hβ and CIV λ1549 profile parameter comparison as a function of luminosity. *Top panels*: behavior of FWHM CIV λ1549 and Hβ (upper half) and of the ratio FWHM(CIV λ1549)/FWHM(Hβ) as a function of L (lower half), for FOS (golden and pale blue) and HE sample (red and blue). The yellow band identifies the region where FWHM(CIV λ1549)/FWHM(Hβ) = 1 within the errors. *Middle panels*: $c\left(\frac{1}{2}\right)$ of Hβ and CIV λ1549 (upper half), and difference $\delta\left(\frac{1}{2}\right)$ as a function of L (lower half). Square symbols indicate Pop. B, circles Pop. A. Lines trace an unweighted least-squares fit for the Pop. A (black) and for Pop. B (red) sources. *Bottom panels*: as in top panels but for $c\left(\frac{1}{4}\right)$ and $\delta\left(\frac{1}{4}\right)$. The vertical dotted lines join Hβ and CIV λ1549 parameters for the same object (e.g., they are not error bars).

thick disk, and its dynamics is dominated by radiation pressure, HILs such as CIV λ1549 emitted in the wind would show the largest blueshifts (if the receding part of the flow is shielded from view). The case of I Zw 1 provided a prototypical case in which a flattened LIL-emitting systems and a radial outflow could be seen at small inclination (e.g., Marziani et al. 1996; Leighly 2004).

From a more modern perspective, there are several indications that the low-ionization BLR is a flattened system (Mejía-Restrepo et al. 2017, 2018a; Negrete et al. 2017, 2018). We see the clearest evidence at the MS extrema: extreme Pop. B sources radiating at very low $L/L_{\rm Edd}$ frequently show LIL profiles consistent with geometrically thin accretion disk profiles (e.g., Chen & Halpern 1989; Strateva et al. 2003; Storchi-Bergmann et al. 2017), which may be hidden in the majority of Pop. B sources (Bon et al. 2007, 2009). A highly flattened LIL-BLR is also suggested in blazars, which are also Pop. B low-radiatiors (Decarli et al. 2011), by comparing the virial product to mass estimates obtained from the correlation between $M_{\rm BH}$ and the host galaxy luminosity. At the other end of the MS, extreme Pop. A quasars show deviations from virial luminosity estimates consistent with the effect of orientation on the line width, if the emitting region is highly flattened (Negrete et al. 2018). A flattened low-ionization BLR is also suggested by comparing the virial product to mass estimates obtained from accretion disk fits to the SED (Mejía-Restrepo et al. 2017, 2018a).

The effect of orientation on the FWHM and on $M_{\rm BH}$ and $L/L_{\rm Edd}$ estimates can be computed by assuming that we are observing randomly oriented samples of quasars whose line emission arises from a flattened structure – possibly the accretion disk itself. The probability of viewing the structure with an isotropic velocity broadening $\delta v_{\rm iso}$ at an angle θ between line-of-sight and the symmetry axis of a flattened structure is $P(\theta) = \sin(\theta)$. The radial velocity spread (in the following we use the FWHM as a measure, $\delta v_{\rm obs} = FWHM$) can be written as

$$\frac{FWHM^2}{4} = \delta v_{\rm iso}^2 + \delta v_{\rm K}^2 \sin^2\theta, \tag{9}$$

which implies that

$$\frac{M_{\rm BH,obs}}{M_{\rm BH,K}} = \frac{\delta v_{\rm obs}^2}{\delta v_{\rm K}^2} = 4 \cdot (\kappa^2 + \sin^2\theta), \tag{10}$$

where $\kappa = \delta v_{\rm iso}/\delta v_{\rm K}$. From Eq. (9) one can estimate the ratio of $\delta v_{\rm obs}$ to intrinsic velocity $\delta v_{\rm K}$ either by computing the most probable value of θ or by deconvolving the observed velocity distribution from $P(\theta)$. The calculations are described in Appendix B. The average ratio is $\langle \frac{M_{\rm BH,obs}}{M_{\rm BH,K}} \rangle \approx 1.1$ if $\kappa = 0.1$. If the FWHM of the Hβ line is used, the $M_{\rm BH}$ suffers from a small bias if the LIL-emitting region is highly flattened. If $\kappa = 0.5$ (a "fat" emitting region), then the bias is much larger $\langle \frac{M_{\rm BH,obs}}{M_{\rm BH,K}} \rangle \approx 2.1$. The $M_{\rm BH}$ dispersion in the case of $\kappa = 0.1$ was estimated for large samples (10^6 replications) with θ distributed according to $P(\theta)$ (Appendix C), and was found to be $\sigma_{M_{\rm BH}} \approx 0.33$ dex. Therefore, even if $P(\theta)$ strongly disfavors cases with $\theta \to 0$, the viewing angle can account for a large fraction of the dispersion in the $M_{\rm BH}$ scaling laws with line width and luminosity.

5.3. A wind component

The interpretation of the CIV λ1549 profile (and Hβ profile differences) rests on the main results of Paper I: the CIV λ1549 shifts are dependent on $L/L_{\rm Edd}$ and, to a lesser extent on L; the CIV λ1549 broadening is due to a blueshifted component whose strength with respect to a virialized component increases with $L/L_{\rm Edd}$ and L.

At one quarter and one half of the fractional intensity the difference in the line centroid radial velocity of Hβ and CIVλ1549, that is, $c\left(\frac{1}{2}\right)$(H$\beta$) – $c\left(\frac{1}{2}\right)$(CIV$\lambda$1549) and $c\left(\frac{1}{4}\right)$(H$\beta$) – $c\left(\frac{1}{4}\right)$(CIV$\lambda$1549), is almost always positive, and can reach 7000 km s^{-1} and 4000 km s^{-1} in the HE sample and FOS, respectively, mainly because of the large CIVλ1549 blueshifts (Fig. 9). A luminosity dependence of $\delta\left(\frac{1}{2}\right) = c\left(\frac{1}{2}\right)$(H$\beta$) – $c\left(\frac{1}{2}\right)$(CIV$\lambda$1549) and $\delta\left(\frac{1}{4}\right) = c\left(\frac{1}{4}\right)$(H$\beta$) – $c\left(\frac{1}{4}\right)$(CIV$\lambda$1549) is illustrated in Fig. 9. The centroid separations are correlated with L, with a similar slope at both one quarter and one half of the fractional intensity (Fig. 9): for $\delta\left(\frac{1}{2}\right)$ of Pop. A,

$$\delta\left(\frac{1}{2}\right) \approx (648 \pm 121)\log L - (28530 \pm 5600)\,\mathrm{km s^{-1}}, \quad (11)$$

in the range $44 \lesssim \log L \lesssim 48.5$.

The trends of Fig. 9 suggest that the CIVλ1549 broadening is however affected by $M_{\rm BH}$, as both the Hβ and CIVλ1549 widths steadily increase with luminosity, and their ratio shows no strong dependence on luminosity. This may be the case if the outflow velocity is a factor k of the virial velocity ($k = \sqrt{2}$ would correspond to the escape velocity). The correlation between shift and FWHM of Paper I indicates that we are seeing an outflow component "emerging" on the blue side of the BC. If we assume that line emission arises from a flattened structure with velocity dispersion $v_{\rm iso}$ (i.e., as in Eq. (9)), and that the outflowing component from the accretion disk contributes to an additional broadening term proportional to $\cos\theta$ (the projection along the line of sight of the outflow velocity), then the observed CIVλ1549 broadening can be written as

$$FWHM^2_{\rm CIV} = 4(\delta v^2_{\rm iso} + \delta v^2_{\rm K}\sin^2\theta) + \daleth^2 \delta v^2_{\rm K} \mathcal{M}\frac{L}{L_{\rm Edd}}\cos^2\theta, \quad (12)$$

where $\daleth$ is a proportionality constant, and $\mathcal{M}$ the force multiplier. It follows that the total broadening can easily exceed $\delta v_{\rm K}$ for a typical viewing angle $\theta = \pi/6$, provided that the factor $Q = \daleth^2 \mathcal{M}\frac{L}{L_{\rm Edd}}$ is larger than 1. The factors $\daleth$ and $\mathcal{M}$ depend on physical properties (density, ionization level) and should be calculated in a real physical model linking ionization condition and dynamics. The factor Q encloses the dependence of wind properties on radiation forces, opacity, and so on (Stevens & Kallman 1990) along with the dependence on ionization. For example, in the case of optically thick gas being accelerated by the full absorption of the ionizing continuum, the force multiplier is $\mathcal{M} = \frac{\alpha}{\sigma_{\rm T} N_{\rm c}} \approx 7.5$ for column density $N_{\rm c} = 10^{23}\,\mathrm{cm^{-2}}$, and $\alpha = 0.5$ (α is the fraction between the ionizing and bolometric luminosity, Netzer & Marziani 2010). If $L/L_{\rm Edd} \rightarrow 1$, and $\daleth \sim 1$, implying $Q \sim O(10)$, the FWHM$_{\rm CIV}$ can exceed the FWHM(Hβ) by up to a factor of several, as indeed observed in the most extreme radiators from the comparison between CIVλ1549 and Hβ.

Equations (9) and (12) account for the consistent increase in broadening of CIVλ1549 and Hβ (Fig. 9). In the context of the present sample covering a wide range in luminosity, L can be considered a proxy for the increase in $M_{\rm BH}$ ($L \propto M_{\rm BH}$, with a scatter set by the $L/L_{\rm Edd}$ distribution) and therefore in Keplerian velocity. The top and middle panels of Fig. 9 show a consistent increase of the centroid, and of the centroid difference $\delta\left(\frac{1}{2}\right)$ and $\delta\left(\frac{1}{4}\right)$ with L. This result motivated the introduction of a luminosity-dependent correction to the line width. The centroid difference can be written as

$$\delta\left(\frac{i}{4}\right) \sim \frac{1}{2}\delta v_{\rm K}\left(\frac{i}{4}\right)\cos\theta\left(-\daleth\left(M\frac{L}{L_{\rm Edd}}\right)^{\frac{1}{2}} + f\right), \; i = 1, 2, \quad (13)$$

with $f \equiv 0$ for Pop. A, and f defined by the infall velocity $v_{\rm inf} = f\delta v_{\rm K}$ as a fraction of the radial free-fall velocity for Pop. B. Equations (13) and (12) imply that $FWHM^2_{\rm CIV} = FWHM^2_{\rm H\beta} + 4\delta^2\left(\frac{1}{2}\right)$, if $f = 0$.

If we ascribe the redward displacement of the Hβ wing in Pop. B sources to gravitational and transverse redshift (e.g., Corbin 1990; Bon et al. 2015),

$$\delta\left(\frac{i}{4}\right) = \frac{1}{2}\left(-\delta v_{\rm K}\left(\frac{i}{4}\right)\daleth\left(\mathcal{M}\frac{L}{L_{\rm Edd}}\right)^{\frac{1}{2}}\cos\theta + \frac{3}{2}cz_{\rm g}\left(\frac{i}{4}\right)\right) \quad (14)$$

$$= \frac{1}{2}\delta v_{\rm K}\left(\frac{i}{4}\right)\left(-\daleth\left(\mathcal{M}\frac{L}{L_{\rm Edd}}\right)^{\frac{1}{2}}\cos\theta + \frac{3}{2}\frac{\delta v_{\rm K}\left(\frac{i}{4}\right)}{c}\right),$$

where $cz_{\rm g} \sim cGM_{\rm BH}/c^2 r$ is the $c\left(\frac{1}{2}\right)$ or $c\left(\frac{1}{4}\right)$ of Hβ, which can usually be 0 (Pop. A) or ≥0 (Pop. B), and where we have used the weak field approximation for the gravitational redshift.

Equations (13) and (14) account for the steady increase in the centroid difference δ with luminosity. The Hβ centroid displacement in Pop. B may be associated with free fall or gravitational redshift. The amplitude of blueshift depends on luminosity in Pop. A. The point is that both Hβ redward displacement and blueshift of CIVλ1549 (and hence their differences) are proportional to the $\delta v_{\rm K}$ and hence to the $M_{\rm BH}$.

The $\xi_{\rm CIV}$ factor can be written as

$$\xi_{\rm CIV} = \left(\frac{\delta v^2_{\rm iso} + \delta v^2_{\rm K}\sin^2\theta}{4(\delta v^2_{\rm iso} + \delta v^2_{\rm K}\sin^2\theta) + \daleth^2\delta v^2_{\rm K}\mathcal{M}\frac{\mathcal{L}}{\mathcal{L}_{\rm Edd}}\cos^{\in}\theta}\right)^{\frac{1}{2}}$$

$$= \left(\frac{1}{1 + \frac{Q\cos^2\theta}{4(\kappa^2+\sin^2\theta)}}\right)^{\frac{1}{2}}. \quad (15)$$

The $\xi_{\rm CIV}$ behavior as a function of the viewing angle θ is described in the top panel of Fig. 10. The figure shows the dependence in the case of a flat $\kappa = 0.1$ (black) or fat $\kappa = 0.5$ (red) for four values of Q. The bottom panel of Fig. 10 shows the behavior of the ratios $\tilde{\xi}_{\rm H\beta} = 1/[4(\kappa^2 + \sin^2\theta)]^{1/2}$ and $\tilde{\xi}_{\rm CIV} = 1/(4\kappa^2 + 4\sin^2\theta + Q\cos^2\theta)^{1/2}$. The $\tilde{\xi}$ are the ratios between the $\delta v_{\rm K}$ and the observed FWHM. At low θ, the FWHM(Hβ) underestimates the $\delta v_{\rm K}$ by a large factor, while the overestimation of $\delta v_{\rm K}$ by the FWHM(CIVλ1549) is almost independent of θ and a factor ≈2.

The panels of Fig. 11 compare the observed distribution of $\xi_{\rm CIV,1}$ (shaded histogram) with the prediction of randomly oriented synthetic samples, at different Q. We are not seeking a fit of the observed distribution especially around $\xi_{\rm CIV} \approx 1$ because of the many biases affecting our sample and of the problem raised by $\xi_{\rm CIV} > 1$ (see below), but a qualitative consistency in the distribution of $\xi_{\rm CIV} < 1$.

If we focus the analysis of Fig. 11 mainly on large shifts, the presence of low $\xi_{\rm CIV}$ values and their higher frequency favors a highly flattened low-ionization BLR, as well as high Q for the full sample. A fat $\kappa = 0.5$ BLR is unable to reproduce the largest shift amplitudes. The scatter in $\xi_{\rm CIV}$ linear values at $Q \gtrsim 2$ is ≈ 0.2, implying a dispersion in the $M_{\rm BH}$ of ≈0.15 dex. If we separate Pop. A and B, more extreme values of $Q \gtrsim 2$ are required to fit the large shift distribution in Pop. A, with $Q \sim 10$. The distribution of $\xi_{\rm CIV}$ for Pop. B is more peaked around $\xi_{\rm CIV} \approx 1$, and the $\xi_{\rm CIV}$ distribution can be qualitatively accounted for if $Q \lesssim 2$.

The $\xi_{\rm CIV}$ observed distribution includes values >1. These values are not possible following our model: the FWHM(CIVλ1549) should be always in excess of or comparable

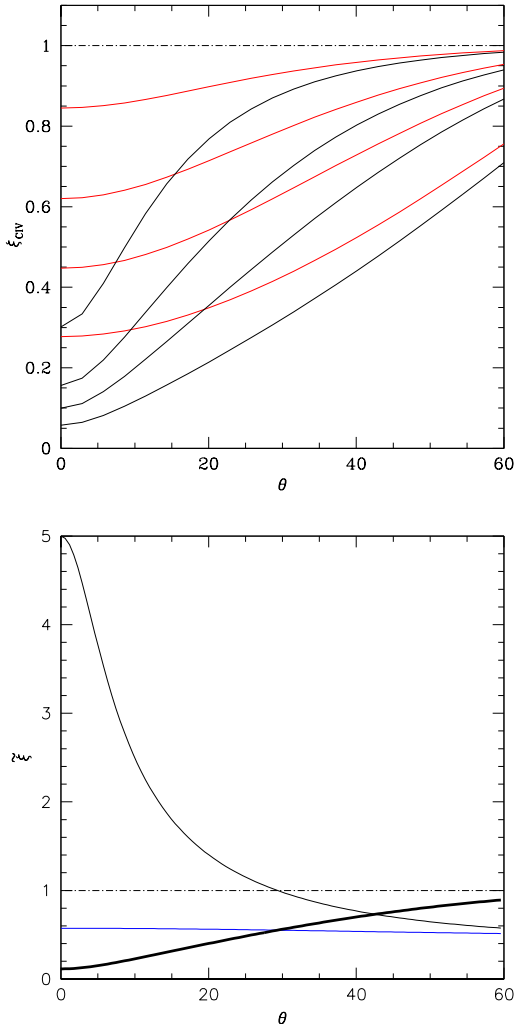

Fig. 10. *Top panel*: parameter $\xi_{\rm CIV}$ behavior as a function of viewing angle as a function of θ for a "thin" emitting region with $\kappa = 0.1$, for different Q values (0.4, 1.6, 4.0, 12.0; black lines). Red line: $\xi_{\rm CIV}$ behavior for a thick emitting region $\kappa = 0.5$, for the same Q values. *Bottom panel*: as in top panel but for $\kappa = 0.1$, with $Q = 12$. The thin lines are the $\tilde{\xi}$ values for Hβ (black) and C IVλ1549 (blue). See text for more details. The thick line is their ratio (also shown in the *top panel*).

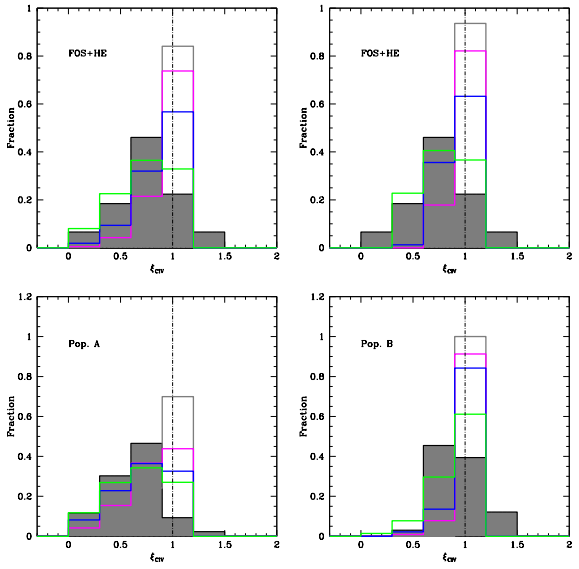

Fig. 11. *Top left*: observed distribution of $\xi_{\rm CIV}$ for the full FOS+HE sample (shaded histogram), and distribution of $\xi_{\rm CIV}$ for $Q = 0.4$ (gray), 0.8 (magenta), 2.0 (blue), and 7.8 (green), assuming $\kappa = 0.1$, for randomly oriented synthetic samples. *Top right*: as in top-left panel but for $\kappa = 0.5$. *Bottom left*: distribution of $\xi_{\rm CIV}$ restricted to Pop. A sources for $Q = 1.0$ (gray), 2.0 (magenta), 4.0 (blue), and 12.0 (green), for $\kappa = 0.1$. *Bottom right*: as in bottom-left but for Pop. B sources, with $Q = 0.$ (gray),0.2 (magenta), 0.4 (blue), and 1.6 (green), for $\kappa = 0.1$. See text for more details.

to FWHM(H$\beta_{\rm BC}$). In the case of $Q \gg 1$, the C IVλ1549 line is broadened by an outflowing component; if $Q \to 0$, $\xi_{\rm CIV} \lesssim 1$. In the latter case, the excess broadening may come from the smaller emissivity-weighted distance expected for C IVλ1549 in a virial velocity field. The existence of cases with FWHM C IVλ1549 < FWHM Hβ was already noted by Mejía-Restrepo et al. (2018b), and therefore it is not unique to the FOS+HE sample. The bottom-right panel of Fig. 11 shows that such cases are relatively frequent among Pop. B. Inspection of the HE spectra in Paper I reveals that the C IVλ1549 profile is significantly affected by semi-broad absorptions such as the ones often found in mini-BAL quasars (Vestergaard 2003; Sulentic et al. 2006b). Since mini-BALs cluster around the line core, it is most likely that these Pop. B sources would satisfy the condition FWHM C IVλ1549 $\gtrsim$ FWHM Hβ if the effect of the absorptions could be removed.

5.4. M_{BH} scaling laws dependent on L/L_{Edd} and L

The goal is to obtain an $M_{\rm BH}$ estimator based on C IVλ1549 that is consistent with the scaling law derived for Hβ. In this context, the dependence on luminosity of FWHM C IVλ1549 cannot be ignored especially if samples encompass a broad range in luminosity. This will be the case in deep, forthcoming surveys. Considering the corrections to FWHM C IVλ1549 of Sect. 4, the $M_{\rm BH}$ scaling law is derived in the form $\log M_{\rm BH} = \alpha \cdot \log L + 2 \cdot \log FWHM + \gamma$ by minimizing the scatter and any systematic deviation of $M_{\rm BH}$ estimated from C IVλ1549 with respect to the Hβ-derived masses: the unweighted least-square fit of Fig. 12 yields

$$M_{\rm BH}({\rm CIV}) \approx (0.99 \pm 0.04) M_{\rm BH}({\rm H}\beta) + (0.11 \pm 0.39). \quad (16)$$

The C IVλ1549 scaling law, with $M_{\rm BH}$ in solar units and L_{1450} normalized by 10^{44}, takes the form:

$$\log M_{\rm BH,1}\,{\rm CIV} \approx (0.64^{+0.045}_{-0.025}) \log L_{1450,44} + 2 \log (\xi_{\rm CIV,1} FWHM({\rm CIV})) + (0.525^{+0.22}_{-0.18}) \quad (17)$$

for the FWHM correction using Eq. (6). Applying Eq. (7), the scaling law does not change appreciably, and uncertainties in the coefficients are only slightly different.

$$\log M_{\rm BH,2}\,{\rm CIV} \approx (0.63^{+0.045}_{-0.035}) \log L_{1450,44} + 2 \log (\xi_{\rm CIV,2} {\rm FWHM(CIV)}) + (0.525^{+0.275}_{-0.19}). \quad (18)$$

The scaling law parameter uncertainties have been estimated following the standard approach in Bevington & Robinson (2003, p. 210ff), with the constraint that unbiased consistency between $M_{\rm BH}$ from Hβ and C IVλ1549 (Eq. (16)) is satisfied within the 1σ uncertainties. The rms scatter is $\sigma \approx 0.33$ for Eq. (6) and $\sigma \approx 0.35$ for Eq. (7). Assuming a single correction for both Pop. A and B significantly worsens the fit quality, and no scaling law is reported.

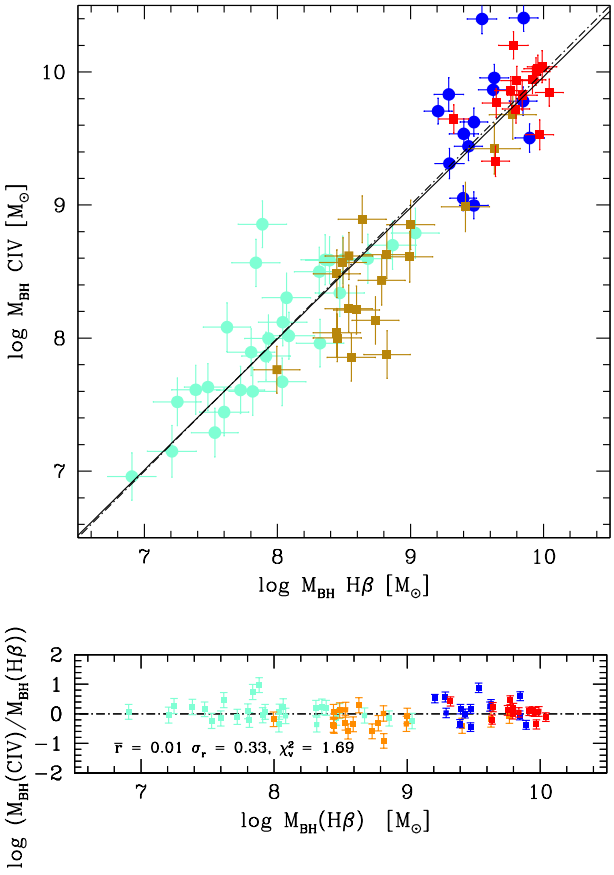

Fig. 12. $M_{\rm BH}$ computed from the fiducial relation of Vestergaard & Peterson (2006) based on FWHM Hβ vs. the one computed from the CIVλ1549 FWHM corrected following Eq. (6). Error bars include luminosity uncertainties estimated by the scatter in L derived from the UV and the visual spectral ranges along with errors on FWHM propagated quadratically. *Lower panel*: residuals for the three cases. Meaning of the color-code is the same as in the previous Figs.

An application of the bisector-fitting technique using SLOPES (Feigelson & Babu 1992) yields

$$\log M_{\rm BH,1}\,{\rm CIV} \approx (0.5925^{+0.0275}_{-0.030})\log L_{1450,44} + 2\log(\xi_{\rm CIV,1} FWHM({\rm CIV})) + (0.62 \pm 032), \quad (19)$$

$$\log M_{\rm BH,2}\,{\rm CIV} \approx (0.572^{+0.0285}_{-0.032})\log L_{1450,44} + 2\log(\xi_{\rm CIV,2} FWHM({\rm CIV})) + (0.64 \pm 035). \quad (20)$$

The Vestergaard & Peterson (2006) Hβ scaling laws suffer from significant scatter (see the discussion in their paper) that can be explained on the basis of the scatter induced by orientation (0.33 dex at 1σ) according to the results of Appendix B. The CIVλ1549 and Hβ relation should be considered equivalent. The luminosity exponent (≈ 0.64) is in agreement with previous observations (Peterson et al. 2005). It is slightly above the exponent of the CIVλ1549 radius dependence on luminosity found in more recent reverberation mapping studies ($\approx$0.52−0.55 Kaspi et al. 2007; Lira et al. 2017, 2018).

Figure 12 suggests the presence of a well-behaved distribution with a few outlying points. It is possible to reduce the scatter to $\sigma \approx 0.25$ applying a σ clipping algorithm (i.e., eliminating all sources deviating more than $\pm 2\sigma$), with no significant change in the best-fit parameters. This selective procedure is however unwarranted: as shown in Appendix C, outlying points are expected precisely because of the possible occurrence of low-probability viewing angles. The residual rms can be largely accounted for by orientation effects if Q is small, and by the combination of orientation effects and outflow prominence if Q is much larger than 1 (Appendix C).

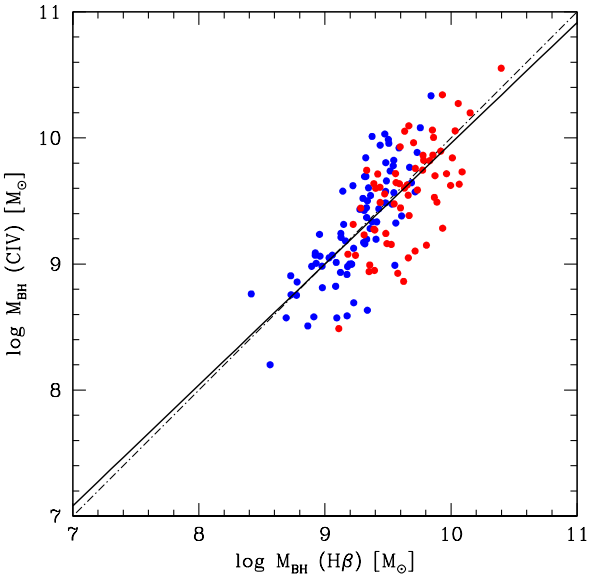

Fig. 13. Estimates of $M_{\rm BH}$ using corrected CIVλ1549 FWHM as a VBE versus $M_{\rm BH}$ computed from Hβ FWHM using the scaling law of Vestergaard & Peterson (2006). The luminosity and FWHM(CIVλ1549) data from Coatman et al. (2017) for Pop. A (blue) and B sources (red; see Sect. 5.5 for more details) are used to compute the CIVλ1549 $M_{\rm BH}$ according to Eq. (17). The dot-dashed line traces the 1:1 relation between $M_{\rm BH}$ from CIVλ1549 and Hβ; the black line is an unweighted least-squares fit for the A+B $M_{\rm BH}$ estimates.

5.5. Application to a large sample with Hβ and CIVλ1549 data

The Coatman et al. (2017) data provide a different sample for the testing of the scaling law of Eq. (17). The flux bisector can be converted into $c\left(\frac{1}{4}\right)$ (Sect. 4.5). An application of Eq. (17) to Pop. A and B (applying the luminosity-dependent separation as in Paper I) yields agreement with the expectation of an unbiased $M_{\rm BH}$ estimator with respect to the Hβ $M_{\rm BH}$ estimates using the scaling law of Vestergaard & Peterson (2006): the slope of an unweighted least-squares fit is $\approx$0.958 ± 0.065 (using SLOPES, Feigelson & Babu 1992, Fig. 13).

6. Conclusion

The present investigation focuses on the CIVλ1549 relations to Hβ over a broad range of luminosities ($\log L \sim 43$−48, including very high luminosities, $\log L \gtrsim 47$) in the Eigenvector 1 context, with the goal of testing the CIVλ1549 suitability as virial broadening estimators when observations of low-ionization lines are not available. The Eigenvector 1 context means that the quasar main sequence is considered to properly interpret first-order Eddington ratio effects and luminosity effects that appear to be second order in low- redshift samples.

The main conclusions that we draw from this study are as follows.

1. Within the limits of our sample size, and of our UV spectral coverage, it does not appear that the CIVλ1549 FWHM can

be used as a reliable virial broadening estimator without significant corrections. There is large scatter between FWHM measurements on Hβ and C IVλ1549 that seems to defy the definition of a meaningful trend.

2. The C IVλ1549$_{\rm NC}$ removal improves the agreement between C IVλ1549 and Hβ measurements in the HE sample, but C IVλ1549$_{\rm NC}$ is not a major factor hampering the definition of a C IVλ1549 VBE consistent with Hβ.

3. Corrections to FWHM C IVλ1549- and C IVλ1549-based $M_{\rm BH}$ estimates that vary systematically along the 4DE1 sequence and are strongly dependent on Eddington ratio are promising and should be further explored.

4. Following the results of Paper I, we define a correction to the FWHM(C IVλ1549) based on the full-profile C IVλ1549 $c\left(\frac{1}{2}\right)$ (a proxy for $L/L_{\rm Edd}$) and on the luminosity at 1450 Å. Given the intrinsic differences between Pop. A and B, and their "threshold" separation dependent on a critical $L/L_{\rm Edd}$, two different correction laws were considered for the two populations. We note that the correction for Pop. B as derived from the FOS+HE sample is highly uncertain.

5. The $M_{\rm BH}$ scaling law (Eq. (17)) associated with the corrected FWHM(C IVλ1549) following Eq. (6), as explained in Sect. 5.4, allows for the preservation of the virial dependence on line broadening. Its practical usefulness rests on the ability to distinguish Pop. A and B quasars. This can be achieved in a large fraction of quasars following the guideline set forth by Negrete et al. (2014).

6. We constructed a toy model that helped the interpretation of the scatter. Orientation effects induce scatter ≈0.3−0.4 dex in mass estimates that account for a large fraction of the dispersion in the landmark scaling law of Vestergaard & Peterson (2006). A physical model of the disk + wind system might allow for the viewing angle θ to be recovered for individual quasars.

Acknowledgements. The authors acknowledge the contribution of Jack Sulentic to the development of this paper which is based on observations made with ESO Telescopes at the Paranal Observatory under programme 082.B-0572(A), and with the Italian Telescopio Nazionale Galileo (TNG) operated on the island of La Palma by the Fundación Galileo Galilei of the INAF at the Spanish Observatorio del Roque de los Muchachos of the Instituto de Astrofísica de Canarias.. PM acknowledges the Programa de Estancias de Investigación (PREI) No. DGAP/DFA/2192/2018 of UNAM, where this paper was completed. The relevant research is part of the projects 176001 "Astrophysical spectroscopy of extragalactic objects" and 176003 "Gravitation and structure of universe on large scales" supported by the Ministry of Education, Science and Technological Development of the Republic of Serbia. MLMA acknowledges a CONACyT postdoctoral fellowship, and wishes to thank the IAA for support during her postdoctoral stay from February 2016 to July 2018. MLMA acknowledges a CONACyT postdoctoral fellowship and National Science Centre, Poland, grant No.2017/26/A/ST9/00756 (Maestro 9). AdO and MLMA acknowledge financial support from the Spanish Ministry of Economy and Competitiveness through grant AYA2016-76682-C3-1-P. AdO acknowledges financial support from the State Agency for Research of the Spanish MCIU through the "Center of Excellence Severo Ochoa" award for the Instituto de Astrofísica de Andalucía (SEV-2017-0709). MLMA, PM and MDO acknowledge funding from the INAF PRIN-SKA 2017 program 1.05.01.88.04. DD and AN acknowledge support from CONACyT through grant CB221398. DD also thanks for support from grants IN108715 and IN113719 PAPIIT, DGAPA, UNAM. MAMC was partially supported by the Spanish Research project MTM2015-64095-P and by Diputación General de Aragón, Group E24-17R. The scientific results reported in this article are also based on publicly available HST spectra.

References

Assef, R. J., Denney, K. D., Kochanek, C. S., et al. 2011, ApJ, 742, 93
Bañados, E., Venemans, B. P., Mazzucchelli, C., et al. 2018, Nature, 553, 473
Bachev, R., Marziani, P., Sulentic, J. W., et al. 2004, ApJ, 617, 171
Baldwin, J. A., Ferland, G. J., Korista, K. T., et al. 1996, ApJ, 461, 664
Bensch, K., del Olmo, A., Sulentic, J., Perea, J., & Marziani, P. 2015, JApA, 36, 467
Bevington, P. R., & Robinson, D. K. 2003, Data Reduction and Error Analysis for the Physical Sciences (McGraw-Hill)
Bischetti, M., Piconcelli, E., Vietri, G., et al. 2017, A&A, 598, A122
Bisogni, S., di Serego Alighieri, S., Goldoni, P., et al. 2017, A&A, 603, A1
Boller, T., Brandt, W. N., & Fink, H. 1996, A&A, 305, 53
Bon, E., Popović, L., & Gavrilović, N. 2007, in Spectral Line Shapes in Astrophysics, eds. L. C. Popovic, & M. S. Dimitrijevic, AIP Conf. Ser., 938, 59
Bon, E., Popović, L. Č., Gavrilović, N., Mura, G. L., & Mediavilla, E. 2009, MNRAS, 400, 924
Bon, N., Bon, E., Marziani, P., & Jovanović, P. 2015, Ap&SS, 360, 7
Boroson, T. A., & Green, R. F. 1992, ApJS, 80, 109
Boyle, B. J., Shanks, T., Croom, S. M., et al. 2000, MNRAS, 317, 1014
Brotherton, M. S., Wills, B. J., Steidel, C. C., & Sargent, W. L. W. 1994a, ApJ, 423, 131
Brotherton, M. S., Wills, B. J., Francis, P. J., & Steidel, C. C. 1994b, ApJ, 430, 495
Brotherton, M. S., Runnoe, J. C., Shang, Z., & DiPompeo, M. A. 2015, MNRAS, 451, 1290
Burbidge, G. R., & Burbidge, E. M. 1967, Quasi-stellar Objects (San Francisco: Freeman)
Chen, K., & Halpern, J. P. 1989, ApJ, 344, 115
Coatman, L., Hewett, P. C., Banerji, M., & Richards, G. T. 2016, MNRAS, 461, 647
Coatman, L., Hewett, P. C., Banerji, M., et al. 2017, MNRAS, 465, 2120
Collin-Souffrin, S., Dyson, J. E., McDowell, J. C., & Perry, J. J. 1988, MNRAS, 232, 539
Corbin, M. R. 1990, ApJ, 357, 346
Corbin, M. R., & Boroson, T. A. 1996, ApJS, 107, 69
Croom, S. M. 2011, ApJ, 736, 161
Czerny, B., & Hryniewicz, K. 2011, A&A, 525, L8
Debuhr, J., Quataert, E., & Ma, C.-P. 2012, MNRAS, 420, 2221
Decarli, R., Dotti, M., & Treves, A. 2011, MNRAS, 413, 39
Denney, K. D., Peterson, B. M., Pogge, R. W., et al. 2010, ApJ, 721, 715
Denney, K. D., Vestergaard, M., Watson, D., & Davis, T. 2012, Am. Astron. Soc. Meeting Abstracts, 219, 440.20
Denney, K. D., Pogge, R. W., Assef, R. J., et al. 2013, ApJ, 775, 60
Denney, K. D., Horne, K., Brandt, W. N., et al. 2016, ApJ, 833, 33
Du, P., Lu, K.-X., Hu, C., et al. 2016, ApJ, 820, 27
Du, P., Zhang, Z.-X., Wang, K., et al. 2018, ApJ, 856, 6
Dultzin-Hacyan, D., Taniguchi, Y., & Uranga, L. 1999, in Structure and Kinematics of Quasar Broad Line Regions, eds. C. M. Gaskell, W. N. Brandt, M. Dietrich, D. Dultzin-Hacyan, & M. Eracleous, ASP Conf. Ser., 175, 303
Elvis, M. 2000, ApJ, 545, 63
Eracleous, M., & Halpern, J. P. 2004, ApJS, 150, 181
Feigelson, E. D., & Babu, G. J. 1992, ApJ, 397, 55
Ferland, G. J., Hu, C., Wang, J., et al. 2009, ApJ, 707, L82
Fine, S., Croom, S. M., Bland-Hawthorn, J., et al. 2010, MNRAS, 409, 591
Flohic, H. M. L. G., Eracleous, M., & Bogdanović, T. 2012, ApJ, 753, 133
Gallerani, S., Fan, X., Maiolino, R., & Pacucci, F. 2017, PASA, 34, e022
Gaskell, C. M. 1982, ApJ, 263, 79
Goad, M. R., & Korista, K. T. 2014, MNRAS, 444, 43
Grier, C. J., Peterson, B. M., Horne, K., et al. 2013, ApJ, 764, 47
Hall, P. B., Hutsemékers, D., Anderson, S. F., et al. 2003, ApJ, 593, 189
Hewett, P. C., & Wild, V. 2010, MNRAS, 405, 2302
Hu, C., Wang, J.-M., Ho, L. C., et al. 2008, ApJ, 683, L115
Hu, C., Wang, J.-M., Ho, L. C., et al. 2012, ApJ, 760, 126
Karouzos, M., Woo, J.-H., Matsuoka, K., et al. 2015, ApJ, 815, 128
Kaspi, S., Brandt, W. N., Maoz, D., et al. 2007, ApJ, 659, 997
Kelly, B. C., & Bechtold, J. 2007, ApJS, 168, 1
Kollatschny, W., & Zetzl, M. 2013, A&A, 549, A100
Kriss, G. 1994, ASP Conf. Ser., 61, 437
Kuraszkiewicz, J., Wilkes, B. J., Schmidt, G., et al. 2009, ApJ, 692, 1180
Kwan, J., & Krolik, J. H. 1981, ApJ, 250, 478
Laor, A., Fiore, F., Elvis, M., Wilkes, B. J., & McDowell, J. C. 1997, ApJ, 477, 93
Latif, M. A., & Ferrara, A. 2016, PASA, 33, e051
Leighly, K. M. 2004, ApJ, 611, 125
Lira, P., Botti, I., Kaspi, S., & Netzer, H. 2017, Front. Astron. Space Sci., 4, 71
Lira, P., Kaspi, S., Netzer, H., et al. 2018, ApJ, 865, 56
Martínez-Aldama, M. L., Dultzin, D., Marziani, P., et al. 2015, ApJS, 217, 3
Martínez-Aldama, M. L., Del Olmo, A., Marziani, P., et al. 2018, Front. Astron. Space Sci., 4, 65
Marziani, P., Sulentic, J. W., Dultzin-Hacyan, D., Calvani, M., & Moles, M. 1996, ApJS, 104, 37
Marziani, P., Sulentic, J. W., Zamanov, R., et al. 2003, ApJS, 145, 199

Marziani, P., Sulentic, J. W., Negrete, C. A., et al. 2010, MNRAS, 409, 1033
Marziani, P., Sulentic, J. W., Plauchu-Frayn, I., & del Olmo, A. 2013a, ApJ, 764, 150
Marziani, P., Sulentic, J. W., Plauchu-Frayn, I., & del Olmo, A. 2013b, A&A, 555, A89
Marziani, P., Martínez Carballo, M. A., Sulentic, J. W., et al. 2016, Ap&SS, 361, 29
Marziani, P., Dultzin, D., Sulentic, J. W., et al. 2018, Front. Astron. Space Sci., 5, 6
Matsuoka, Y., Kawara, K., & Oyabu, S. 2008, ApJ, 673, 62
Matsuoka, K., Silverman, J. D., Schramm, M., et al. 2013, ApJ, 771, 64
McLure, R. J., & Dunlop, J. S. 2004, MNRAS, 352, 1390
McLure, R. J., & Jarvis, M. J. 2002, MNRAS, 337, 109
Mejía-Restrepo, J. E., Trakhtenbrot, B., Lira, P., Netzer, H., & Capellupo, D. M. 2016, MNRAS, 460, 187
Mejía-Restrepo, J. E., Lira, P., Netzer, H., Trakhtenbrot, B., & Capellupo, D. 2017, Front. Astron. Space Sci., 4, 70
Mejía-Restrepo, J. E., Lira, P., Netzer, H., Trakhtenbrot, B., & Capellupo, D. M. 2018a, Nat. Astron., 2, 63
Mejía-Restrepo, J. E., Trakhtenbrot, B., Lira, P., & Netzer, H. 2018b, MNRAS, 478, 1929
Negrete, C. A., Dultzin, D., Marziani, P., & Sulentic, J. W. 2014, ApJ, 794, 95
Negrete, C. A., Dultzin, D., Marziani, P., et al. 2017, Front. Astron. Space Sci., 4, 59
Negrete, C. A., Dultzin, D., Marziani, P., et al. 2018, A&A, 620, A118
Netzer, H. 1990, in Active Galactic Nuclei, eds. R. D. Blandford, H. Netzer, L. Woltjer, T. J.-L. Courvoisier, & M. Mayor, 57
Netzer, H., & Marziani, P. 2010, ApJ, 724, 318
Netzer, H., Lira, P., Trakhtenbrot, B., Shemmer, O., & Cury, I. 2007, ApJ, 671, 1256
Osterbrock, D. E., & Shuder, J. M. 1982, ApJS, 49, 149
Park, D., Woo, J.-H., Denney, K. D., & Shin, J. 2013, ApJ, 770, 87
Pei, L., Fausnaugh, M. M., Barth, A. J., et al. 2017, ApJ, 837, 131
Peterson, B. M. 2014, SpScieRev, 183, 253
Peterson, B. M., & Ferland, G. J. 1986, Nature, 324, 345
Peterson, B. M., & Wandel, A. 1999, ApJ, 521, L95
Peterson, B. M., & Wandel, A. 2000, ApJ, 540, L13
Peterson, B. M., Bentz, M. C., Desroches, L.-B., et al. 2005, ApJ, 632, 799
Plotkin, R. M., Shemmer, O., Trakhtenbrot, B., et al. 2015, ApJ, 805, 123
Proga, D., & Kallman, T. R. 2004, ApJ, 616, 688
Proga, D., Stone, J. M., & Kallman, T. R. 2000, ApJ, 543, 686
Punsly, B. 2010, ApJ, 713, 232
Punsly, B., & Zhang, S. 2011, ApJ, 735, L3
Richards, G. T., Kruczek, N. E., Gallagher, S. C., et al. 2011, AJ, 141, 167
Runnoe, J. C., Brotherton, M. S., DiPompeo, M. A., & Shang, Z. 2014, MNRAS, 438, 3263
Saito, Y., Imanishi, M., Minowa, Y., et al. 2016, PASJ, 68, 1
Sdowski, A., Narayan, R., McKinney, J. C., & Tchekhovskoy, A. 2014, MNRAS, 439, 503
Shang, Z., Brotherton, M. S., Wills, B. J., et al. 2011, ApJS, 196, 2
Shen, Y. 2013, Bull. Astron. Soc. India, 41, 61
Shen, Y. 2016, ApJ, 817, 55
Shen, Y., & Ho, L. C. 2014, Nature, 513, 210
Shen, Y., & Liu, X. 2012, ApJ, 753, 125
Shen, Y., Brandt, W. N., Richards, G. T., et al. 2016, ApJ, 831, 7
Snedden, S., & Gaskell, C. 2004, in AGN Physics with the Sloan Digital Sky Survey, eds. G. T. Richards, & P. B. Hall, ASP Conf. Ser., 311, 197
Snedden, S. A., & Gaskell, C. M. 2007, ApJ, 669, 126
Steinhardt, C. L., & Silverman, J. D. 2013, PASJ, 65, 82
Stevens, I. R., & Kallman, T. R. 1990, ApJ, 365, 321
Storchi-Bergmann, T., Schimoia, J. S., Peterson, B. M., et al. 2017, ApJ, 835, 236
Strateva, I. V., Strauss, M. A., Hao, L., et al. 2003, AJ, 126, 1720
Sulentic, J. W. 1989, ApJ, 343, 54
Sulentic, J., & Marziani, P. 2015, Front. Astron. Space Sci., 2, 6
Sulentic, J. W., Marziani, P., & Dultzin-Hacyan, D. 2000a, ARA&A, 38, 521
Sulentic, J. W., Marziani, P., Zwitter, T., Dultzin-Hacyan, D., & Calvani, M. 2000b, ApJ, 545, L15
Sulentic, J. W., Zwitter, T., Marziani, P., & Dultzin-Hacyan, D. 2000c, ApJ, 536, L5
Sulentic, J. W., Marziani, P., Zamanov, R., et al. 2002, ApJ, 566, L71
Sulentic, J. W., Stirpe, G. M., Marziani, P., et al. 2004, A&A, 423, 121
Sulentic, J. W., Repetto, P., Stirpe, G. M., et al. 2006a, A&A, 456, 929
Sulentic, J. W., Dultzin-Hacyan, D., Marziani, P., et al. 2006b, Rev. Mex. Astron. Astrofis., 42, 23
Sulentic, J. W., Bachev, R., Marziani, P., Negrete, C. A., & Dultzin, D. 2007, ApJ, 666, 757
Sulentic, J., Marziani, P., & Zamfir, S. 2011, Balt. Astron., 20, 427
Sulentic, J. W., Marziani, P., del Olmo, A., et al. 2014, A&A, 570, A96
Sulentic, J. W., Martínez-Carballo, M. A., Marziani, P., et al. 2015, MNRAS, 450, 1916
Sulentic, J. W., del Olmo, A., Marziani, P., et al. 2017, A&A, 608, A122
Sun, J., & Shen, Y. 2015, ApJ, 804, L15
Sun, M., Xue, Y., Richards, G. T., et al. 2018, ApJ, 854, 128
Tilton, E. M., & Shull, J. M. 2013, ApJ, 774, 67
Trakhtenbrot, B., & Netzer, H. 2012, MNRAS, 427, 3081
Trevese, D., Perna, M., Vagnetti, F., Saturni, F. G., & Dadina, M. 2014, ApJ, 795, 164
Tytler, D., & Fan, X.-M. 1992, ApJS, 79, 1
Vanden Berk, D. E., Richards, G. T., Bauer, A., et al. 2001, AJ, 122, 549
Vestergaard, M. 2003, ApJ, 599, 116
Vestergaard, M., & Peterson, B. M. 2006, ApJ, 641, 689
Vietri, G. 2017, Am. Astron. Soc. Meeting Abstracts, 229, 302.06
Vietri, G., Piconcelli, E., Bischetti, M., et al. 2018, A&A, 617, A81
Vollmer, B., Schartmann, M., Burtscher, L., et al. 2018, A&A, 615, A164
Wang, J., & Li, Y. 2011, ApJ, 742, L12
Wang, T., Brinkmann, W., & Bergeron, J. 1996, A&Ap, 309, 81
Wang, J., Dong, X., Wang, T., et al. 2009, ApJ, 707, 1334
Wang, H., Wang, T., Zhou, H., et al. 2011, ApJ, 738, 85
Wang, J.-M., Qiu, J., Du, P., & Ho, L. C. 2014a, ApJ, 797, 65
Wang, J.-M., Du, P., Li, Y.-R., et al. 2014b, ApJ, 792, L13
Wang, J.-M., Du, P., Brotherton, M. S., et al. 2017, Nat. Astron., 1, 775
Wills, B. J., Netzer, H., & Wills, D. 1985, ApJ, 288, 94
Wills, B. J., Brotherton, M. S., Fang, D., Steidel, C. C., & Sargent, W. L. W. 1993, ApJ, 415, 563
Wisotzki, L., Christlieb, N., Bade, N., et al. 2000, A&A, 358, 77
Yip, C. W., Connolly, A. J., Vanden Berk, D. E., et al. 2004, AJ, 128, 2603
Yong, S. Y., King, A. L., Webster, R. L., et al. 2018, MNRAS, 479, 4153
Zamanov, R., Marziani, P., Sulentic, J. W., et al. 2002, ApJ, 576, L9
Zamfir, S., Sulentic, J. W., Marziani, P., & Dultzin, D. 2010, MNRAS, 403, 1759

Appendix A: The MS / 4DE1 formalism: a glossary

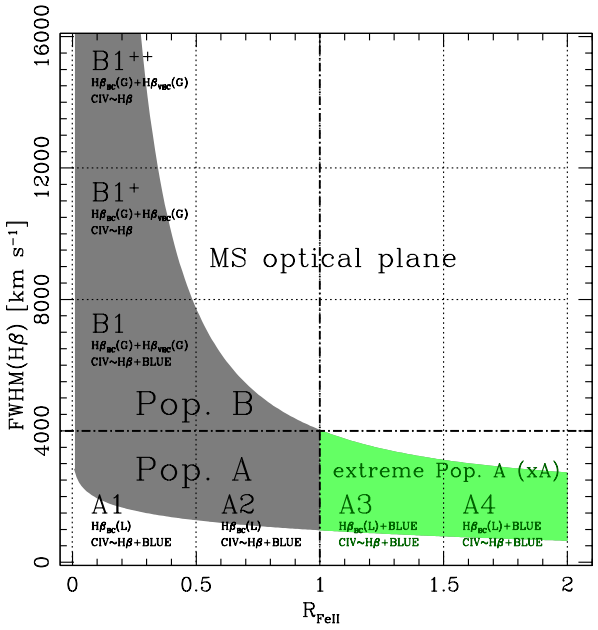

Fig. A.1. Schematic representation of the optical plane of the quasar MS, with the subdivisions identifying spectral types along the sequence. The main components that are blended in the Hβ and Civλ1549 profile are listed in each spectral bin. The shaded area shows the approximate occupation of low-z quasars sample in the plane.

In the optical plane of the quasar main sequence, spectral types are isolated following Sulentic et al. (2002). Figure A.1 provides a sketch and Table A.1 a summary with the spectral types identification in the optical plane of the MS. Here we provide a glossary of the MS-related terms and acronyms employed in the paper, along the order of the quasar main sequence. A more thorough description can be found in Sulentic et al. (2011) and Marziani et al. (2018).

The rational for two type-1 quasar populations (A and B) was originally given by Sulentic et al. (2000a). Spectral types A3 and A4 are also indicated as extreme Population A, with $R_{\rm FeII} \gtrsim 1$. They are the highest radiators per unit mass and possibly super-Eddington accretors (Wang et al. 2014b).

The 4D Eigenvector-1 formalism was introduced to limit the set of MS-correlated parameters to the four ones that are most relevant for the MS physical interpretation. In addition to FWHM Hβ, $R_{\rm FeII}$, and $c\left(\frac{1}{2}\right)$ Civλ1549, the soft X-ray photon index $\Gamma_{\rm soft}$ is also considered (Sulentic et al. 2000b). The four parameters were meant to represent the velocity dispersion of the LIL-emitting part of the BLR, the physical condition within the LIL-BLR ($R_{\rm FeII}$), the dynamical condition of the HIL-emitting gas, and the accretion state of the black hole. $\Gamma_{\rm soft} > 2$ implies a soft X-ray excess that is exclusive of Population A (Wang et al. 1996; Boller et al. 1996; Shen & Ho 2014; Bensch et al. 2015).

Line components assumed in the decomposition along the MS are defined as follows (see also the sketch of Fig. A.1 and Table A.2).

BLUE becomes detectable as a blueward excess in the Hβ profile mainly in A3 and A4 (more infrequently in A2). For Civλ1549, BLUE increases in prominence along the sequence from B1^{++}, to A4. In B1^{++} and B1^{+} is weak and often undetectable, while in A3 and A4 it may dominate Civλ1549 emission.

Table A.1. Spectral type definition along the main sequence.

ST	Definition
	Population B: $FWHM(\mathrm{H}\beta) \gtrsim 4000\,\mathrm{km\,s^{-1}}$. Virial-dominated with redward-asymmetric profiles in Hβ and Mgiiλ2800. Also described a disk-dominated (Richards et al. 2011).
B1++	$12\,000\,\mathrm{km\,s^{-1}} \leq FWHM(\mathrm{H}\beta) < 16\,000\,\mathrm{km\,s^{-1}}$, $R_{\rm FeII} < 0.5$
B1+	$8000\,\mathrm{km\,s^{-1}} \leq FWHM(\mathrm{H}\beta) < 12\,000\mathrm{km\,s^{-1}}$, $R_{\rm FeII} < 0.5$
B1	$4000\,\mathrm{km\,s^{-1}} \leq FWHM(\mathrm{H}\beta) < 8000\mathrm{km\,s^{-1}}$, $R_{\rm FeII} < 0.5$
	Population A: $FWHM(\mathrm{H}\beta) \lesssim 4000\mathrm{km\,s^{-1}}$. Sources frequently show Civλ1549 blueshifts, and Hβ Lorentzian-like profiles (Du et al. 2016). Includes a range of FeII emission.
A1	$FWHM(\mathrm{H}\beta) < 4000\,\mathrm{km\,s^{-1}}$; $R_{\rm FeII} < 0.5$
A2	$FWHM(\mathrm{H}\beta) < 4000\,\mathrm{km\,s^{-1}}$; $\leq 0.5 R_{\rm FeII} < 1$
A3 [xA]	$FWHM(\mathrm{H}\beta) < 4000\,\mathrm{km\,s^{-1}}$; $\leq 1 R_{\rm FeII} < 1.5$
A4 [xA]	$FWHM(\mathrm{H}\beta) < 4000\,\mathrm{km\,s^{-1}}$; $1.5 \leq R_{\rm FeII} < 2$

Table A.2. Line components along the main sequence.

Line component	Definition
	Low-ionization lines (LILs): HI Hβ
H$\beta_{\rm VBC}$	Gaussian $FWHM \sim 10\,000\,\mathrm{km\,s^{-1}}$, redshifted by $1-2000\,\mathrm{km\,s^{-1}}$ (defining property of Pop. B; absent in Pop. A)
H$\beta_{\rm BC}$	Lorentzian, $FWHM \sim 1-4000\,\mathrm{km\,s^{-1}}$ (Pop. A); Gaussian $FWHM\mathrm{H}\beta \gtrsim 4000\,\mathrm{km\,s^{-1}}$ (Pop. B)
Hβ BLUE	Asymmetric Gaussian which models an excess of emission on the blue side of Hβ; usually weak save in ST A3 and A4
Hβ	Sum of H$\beta_{\rm BC}$, H$\beta_{\rm VBC}$, and BLUE (when applicable); full broad Hβ profile
H$\beta_{\rm NC}$	Hβ narrow component
	High-ionization lines (HILs): Civλ1549
Civλ1549$_{\rm VBC}$	Gaussian $FWHM \sim 10\,000\,\mathrm{km\,s^{-1}}$, redshifted by $1-2000\,\mathrm{km\,s^{-1}}$
Civλ1549$_{\rm BC}$	Lorentzian, if $FWHM(\mathrm{H}\beta) \lesssim 4000\mathrm{km\,s^{-1}}$ (Pop. A); Gaussian $FWHM \gtrsim 4000\,\mathrm{km\,s^{-1}}$ (Pop. B)
Civλ1549 BLUE	Asymmetric Gaussian which models an excess of emission on the blue side of Civλ1549; detected in most quasar and most prominent in spectral types A3 and A4
Civλ1549	Sum of Civλ1549$_{\rm BC}$, Civλ1549$_{\rm VBC}$, and Civλ1549 BLUE; full broad Civλ1549 profile
Civλ1549$_{\rm NC}$	Civλ1549 narrow component, prominent in Pop. B at low-z; almost absent in most Pop. A sources

Appendix B: Effect of orientation on Hβ $M_{\rm BH}$ estimates

From the inversion of Eq. (9), we obtain an expression for the viewing angle $\theta = \arcsin\sqrt{x^2/4 - \kappa^2}$, where $x = \delta v_{\rm obs}/\delta v_{\rm K}$ and $\kappa = \delta v_{\rm iso}/\delta v_{\rm K}$. The probability to observe $\delta v_{\rm obs}$ for a given $\delta v_{\rm K}$ is then

$$P(x) = \sqrt{x^2/4 - \kappa^2}\frac{{\rm d}\theta}{{\rm d}x} = \frac{x/4}{\sqrt{\kappa^2 - x^2/4 + 1}}. \quad \text{(B.1)}$$

The black hole mass is $\propto x^2$. Therefore the average effect can be written as

$$\langle\frac{M_{\rm BH,obs}}{M_{\rm BH,K}}\rangle = \int_{x(v_{\rm iso})}^{x({\rm edge})} x^2 P(x){\rm d}x / \int_{x(v_{\rm iso})}^{x({\rm edge})} P(x){\rm d}x. \quad \text{(B.2)}$$

The integrals of Eq. (B.2) can be computed analytically:

$$\int x^2 P(x){\rm d}x = \left(-\frac{4}{3}\sqrt{4\kappa^2 - x^2 + 4}\right) - \frac{4}{3}\kappa^2\sqrt{4\kappa^2 - x^2 + 4} - \frac{1}{6}\left(x^2\sqrt{4\kappa^2 - x^2 + 4}\right), \quad \text{(B.3)}$$

$$\int P(x){\rm d}x = -\sqrt{1 + \kappa^2 - x^2/4}. \quad \text{(B.4)}$$

We note that the integration limits in x (which correspond to $\theta = 0$ and $\theta = 45$) are different for $\kappa = 0.1$ and 0.5. For $\kappa = 0.1$, $x_{\rm iso} = 0.2$ and $x_{\rm edge} \approx 1.43$ In the latter case, $\theta = 0$ corresponds to $x_{\rm min} = 1$ and $\theta = 45$ to $x_{\rm edge} \approx 1.73$: $M_{\rm BH}$ will be always overestimated, for every possible θ value larger than 0.

If we consider the Eddington ratio, we obtain

$$\int P(x)/x^2{\rm d}x = -\,{\rm arctan\,h}\left(\frac{\sqrt{\kappa^2+1}}{\sqrt{\kappa^2 - x^2/4 + 1}}\right)/4\sqrt{\kappa^2+1}. \quad \text{(B.5)}$$

Equation (B.5) implies a significant effect on $L/L_{\rm Edd}$ for both $\kappa = 0.1$ and $\kappa = 0.5$. In the first case, the $L/L_{\rm Edd}$ will be overestimated by a factor ≈ 1.8. In the second case, the $L/L_{\rm Edd}$ will be underestimated by a factor $\approx$2, due to the systematic overestimation in $M_{\rm BH}$.

Appendix C: Origin of scatter in scaling laws

We considered synthetic samples of $\sim$10 000 objects obtained from random variates with distribution $P(\theta) \propto \sin\theta$ ($0 \le \theta \le \pi/4$), and "true" $M_{\rm BH}$ uniformly distributed in the range $10^7\,M_\odot \le M_{\rm BH} \le 10^9\,M_\odot$. The dependence on orientation of the Hβ FWHM is assumed to follow Eq. (9), with $\kappa = 0.1$. The effect of orientation on FWHM is such that in a randomly oriented synthetic sample the $M_{\rm BH}$ estimated from Hβ deviates from the true $M_{\rm BH}$ as in Fig. C.1 (top panel). The dispersion is $\approx$0.35, which is comparable to the uncertainty in the scaling-law $M_{\rm BH}$ estimate following Vestergaard & Peterson (2006, $\approx$0.5 at 1σ confidence level).

The estimates of $M_{\rm BH}$ CIVλ1549 show a significant scatter if plotted against $M_{\rm BH}$ Hβ (Fig. 12). The origin of the scatter is in part related to orientation, in part to the outflow component. The second panel from top of Fig. C.1 shows the $M_{\rm BH}$ CIVλ1549 vs. Hβ for a synthetic sample to which no correction has been applied. FWHM of CIVλ1549 and Hβ are expected to be related to the Keplerian velocity by Eqs. (12) and (10), respectively. The

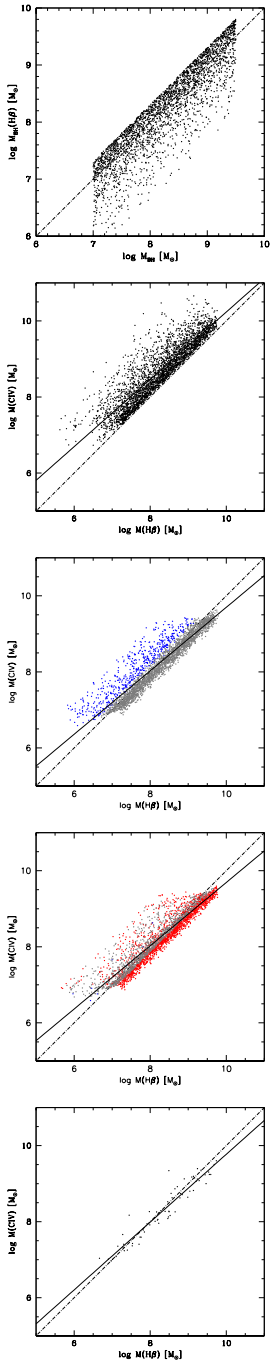

Fig. C.1. *Top*: $M_{\rm BH}$ with effect of orientation via Eq. (10) vs. the "true" $M_{\rm BH}$, for a synthetic sample of 10 000 sources. *Second from top*: $M_{\rm BH}$ CIVλ1549 vs. $M_{\rm BH}$ Hβ estimated for an Eddington ratio distribution as described in the text and no correction. *Third from top*: FWHM $M_{\rm BH}$ CIVλ1549 corrected because of outflow broadening using a correction factor ξ. The blue dots identify the $M_{\rm BH}$ Hβ estimates that are under 0.33 dex the true $M_{\rm BH}$; the red ones are for overestimates by more than 0.33 dex. The gray dots represent mass estimates within -0.33 and $+0.33$ dex from the true value. *Fourth from top*: as above but with color-coding referring to CIVλ1549 $M_{\rm BH}$. *Bottom*: synthetic sample with $n \lesssim 80$ sources, as in the FOS+HE sample. See text for more details. In all panels, the dot-dashed line is the equality line; the filled line traces an unweighted least-squares fit.

distribution of $L/L_{\rm Edd}$ has been assumed Gaussian, peaking at $\log L/L_{\rm Edd} = -0.3$, and $\sigma \approx 0.5$. Typical values of $\xi_{\rm CIV}$ and Q are appropriate for Pop. A sources. There is a strong bias (0.5 dex)

and a standard deviation of the mass ratios of ≈0.6 dex. In some rare instances (a combination of face-on orientation and large outflow velocity) the ratio between $M_{\rm BH}$ from Hβ and CIVλ1549 can reach a factor $\sim 10^2$, as actually found by Sulentic et al. (2007).

The third and fourth panels from the top show the same configuration, but after applying a correction factor $\xi_{\rm CIV}$ in the form $1/\zeta(L, L/L_{\rm Edd}) = 1/(1 + kL^a(L/L_{\rm Edd})^b)$, with $a \approx 0.1$, $b \approx 1$ and no dependence on orientation, intended to mimic the correction actually applied to the data in Sect. 4. The orientation effect is changing the CIVλ1549 FWHM following Eq. (12), and therefore displacing the $M_{\rm BH}$ from the true mass also after correcting the FWHM. We note that the outlying blue points are due to Hβ underestimates of the mass by more than 0.33 dex because of low values of the viewing angle θ. On the contrary, the relatively high value of Q in the simulation produces a significant fraction of $M_{\rm BH}$ CIVλ1549 which are overestimating the $M_{\rm BH}$ by more than 0.33 dex (red points). The dispersion is however reduced with respect to the case with no correction, with an rms $\approx$ 0.3. The bottom panel is a realization of the synthetic sample for a number of sources $\lesssim$100, comparable to the size of the FOS+HE sample, and Gaussian distribution of $L/L_{\rm Edd}$ as for case shown and correction in the second panel from top.

In all of these cases save the one of the second panel from top the dispersion remains ∼0.3, comparable to the one measured for the scaling laws of Eqs. (17) and (18). It is interesting to note that in the framework of the toy model, if $Q = 0$ the orientation-induced scatter is the same for Hβ and CIVλ1549; if $Q \approx 4$, CIVλ1549 becomes an almost perfect VBE, with all the scatter being due to Hβ, in a plot $M_{\rm BH}$ CIVλ1549 vs $M_{\rm BH}$ Hβ. These results may be consistent with no strong dependence on orientation of the CIVλ1549 line shift in RL quasars (Runnoe et al. 2014)[3].

A uniform distribution of Q between 0 and 1.6, a situation more appropriate for Pop. B, was also considered. The results were similar with smaller dispersion and biases.

[3] However, it is not clear whether the results of Runnoe et al. (2014) are applicable to radio quiet quasars: RL sources show no strong evidence of large blueshifts (Sulentic et al. 2007; Richards et al. 2011) as the disk outflow properties may be strongly affected by the powerful radio ejecta (e.g. Punsly 2010; Punsly & Zhang 2011; Sulentic et al. 2015, and references therein).